Notch-dependent DNA *cis*-regulatory elements and their dose-dependent control of *C. elegans* stem cell self-renewal

Tina R Lynch[1,2], Mingyu Xue[1,5], Cazza W. Czerniak[1,4], ChangHwan Lee[1, 3], and Judith Kimble[1,2]

[1]Department of Biochemistry, University of Wisconsin-Madison 53706

[2] Integrated Program in Biochemistry

[3] Department of Biological Sciences, University at Albany, State University of New York, 12222

[4]Joint Department of Biomedical Engineering, Marquette University and Medical College of Wisconsin, Milwaukee, WI 53226

[5]Department of Life Sciences, Imperial College London, South Kensington, London

Running title:

Developmental analysis of CREs

Key words: transcription factor binding site, homotypic cluster, gradient, spatiotemporal resolution, smFISH, *sygl-1*

Summary statement:

Notch-dependent DNA *cis*-regulatory elements work together in their developmental context to shape a transcriptional gradient, control stem cell pool size, and govern differentiation onset.

Abstract

A long-standing biological question is how DNA *cis*-regulatory elements shape transcriptional patterns during metazoan development. The use of reporter constructs, cell culture and computational modeling has made enormous contributions to understanding this fundamental question, but analysis of regulatory elements in their natural developmental context is an essential but rarely used complement. Here, we edited Notch-dependent *cis*-regulatory elements in the endogenous *C. elegans sygl-1* gene, which encodes a key stem cell regulator. We then analyzed the *in vivo* consequences of those mutations – on both gene expression (nascent transcripts, mRNA, protein) and stem cell maintenance. Mutation of a single element in a three-element homotypic cluster reduced expression as well as stem cell pool size by about half, while mutation of two elements essentially abolished them. We find that LBS number and LBS neighborhood are both important to activity: elements on separate chromosomes function additively, while elements in the same cluster act synergistically. Our approach of precise CRISPR/Cas9 gene editing coupled with quantitation of both molecular and biological readouts establishes a powerful model for *in vivo* functional analyses of DNA *cis*-regulatory elements.

Introduction

Cell signaling and transcriptional regulation are central to metazoan development. Though signaling pathways vary tremendously, a common theme is their patterned control of gene expression via DNA *cis*-regulatory elements (CREs). Traditional analyses of signaling rely on manipulations of the pathway's core components (e.g. Austin and Kimble, 1987; Beumer and Clevers, 2021; Lee et al., 2016). Such pathway-level intervention is powerful, but likely impacts multiple target genes and circuits. An alternative approach manipulates signal-dependent CREs in the signaling target gene. Metazoan CREs have been subjected to many elegant analyses over decades, with integration of empirical data and computational modeling being particularly useful (e.g. Andersson and Sandelin, 2020; Bentovim et al., 2017; Ezer et al., 2014; Giorgetti et al., 2010; Lammers et al., 2020; Wong and Gunawardena, 2020). The advent of CRISPR/Cas9 gene editing has now made metazoan CREs accessible in their natural developmental context. The analysis of CREs in endogenous genes has the potential not only to solidify principles gleaned from the classic more artificial experiments but also to advance our understanding of how *cis*-regulatory elements function during development.

Here, we take advantage of a well-established model system to investigate how a cluster of CREs controls development *in vivo*. We focus on Notch-dependent CREs in the *C. elegans sygl-1* gene, which encodes a key regulator of self-renewal in germline stem cells (GSCs) (reviewed in Hubbard and Schedl,

57 2019). In this small nematode, GLP-1/Notch signaling from the niche activates transcription of two target
58 genes, *sygl-1* and *lst-1* (Kershner et al., 2014; Lee et al., 2016; Shin et al., 2017) (Fig. 1A). These genes are
59 functionally redundant: either *sygl-1* or *lst-1* can maintain GSCs on its own, but removal of both genes
60 triggers premature differentiation and loss of GSCs, the Glp phenotype (Fig. 1B) (Kershner et al., 2014).
61 Indeed, *sygl-1* and *lst-1* are likely the only Notch targets responsible for GSC maintenance (Chen et al.,
62 2020). We previously reported that *sygl-1* and *lst-1* transcription is graded in germ cells within the niche
63 (Fig. 1C) (Kershner et al., 2014; Lee et al., 2016), and that SYGL-1 and LST-1 proteins are restricted to a
64 distal region within the progenitor zone (PZ), where GSCs reside (Fig. 1C, yellow) (Haupt et al., 2019; Shin
65 et al., 2017). When SYGL-1 expression is expanded, the GSC pool also expands, suggesting that SYGL-1
66 spatial extent determines where GSC daughters transition from a stem cell state to one primed for
67 differentiation (Shin et al., 2017). However, only *sygl-1* null mutants were available before this work, so
68 the impact of reduced *sygl-1* was unknown.

69 The *sygl-1* gene is well poised for CRE mutational analyses. Its transcription in GSCs relies on signaling
70 by a single pathway, the Notch pathway (Kershner et al., 2014), and its wild-type transcriptional response
71 to Notch signaling has been described at high resolution (Lee et al., 2016). Notch activates transcription
72 via a highly conserved tripartite complex that includes LAG-1, a member of the CSL (CBF1-
73 RBPJκ/Su(H)/LAG-1) family of DNA-binding proteins; the intracellular domain of the Notch receptor
74 (NICD); and the LAG-3/SEL-8 Mastermind-like co-activator (Fig. 1D) (reviewed in Greenwald and Kovall,
75 2013). LAG-1 anchors the complex to DNA at LAG-1 binding sites (LBSs), motifs that are highly conserved
76 for CSL proteins across phylogeny (Christensen et al., 1996; Nellesen et al., 1999; Tun et al., 1994). The
77 *sygl-1* 5' flanking region possesses four computationally predicted LBSs (Fig. 1E) (Yoo et al., 2004).
78 Moreover, a 1 kb *sygl-1* DNA fragment harboring those LBSs drives GFP reporter expression in GSCs
79 (Kershner et al., 2014). Wild-type *sygl-1* transcripts are graded across the GSC pool and become low or
80 undetectable as GSCs are triggered to begin differentiation (Lee et al., 2016) (Fig. 1C). SYGL-1 protein,
81 visualized with a V5 epitope tag, is patterned similarly to *sygl-1* RNA (Shin et al., 2017). Far more proximally
82 in the germline, *sygl-1* transcription becomes independent of Notch signaling (Kershner et al., 2014; Lee
83 et al., 2016). Previous quantitative analyses of Notch-dependent *sygl-1* transcription laid a critical
84 foundation for our investigation of *sygl-1* CRE mutations. Single molecule fluorescence *in situ*
85 hybridization (smFISH) in fixed gonads visualized nascent transcripts at nuclear active transcription sites
86 (ATS) plus cytoplasmic mRNAs, and also showed that a weakened receptor forms a shallower gradient
87 (Lee et al., 2016). Live imaging extended the smFISH results to reveal that the strength of Notch signaling

88 corresponds to the duration of a *sygl-1* transcriptional burst (Lee et al., 2019), a result confirmed by a
89 parallel study in Drosophila embryos (Falo-Sanjuan et al., 2019).
90 Our approach to *in vivo* investigations of CRE function takes advantage of a metazoan exemplary for
91 its relative simplicity and tractability. Multiple and diverse CREs have been implicated in regulation of
92 transcriptional patterns during development, which makes CRE mutations difficult to interpret (Kuang et
93 al., 2021; Li et al., 2021; Park et al., 2019). However, tackling CRE function in a well-defined model like *C.*
94 *elegans*, and the *sygl-1* gene in particular, strips layers of complexity. For example, in flies and mammals,
95 a cooperative physical interaction between neighboring NICD proteins promotes transcriptional synergy
96 when CSL binding sites are spaced ~15-17 bp apart and arranged with head-to-head polarity (Arnett et al.,
97 2010; Bailey and Posakony, 1995; Cave et al., 2005; Kobia et al., 2020; Kuang et al., 2021; Nam et al., 2007;
98 Nellesen et al., 1999; Severson et al., 2017). By contrast, the molecular interface responsible for that NICD
99 interaction is not conserved in nematodes, and LBS polarity is apparently not critical for Notch-dependent
100 expression in *C. elegans* (Nam et al., 2007; Neves et al., 2007). The lack of this cooperative NICD interaction
101 in nematodes removes one layer of complexity and so has potential to reveal principles relevant to
102 homotypic clusters more broadly.
103 Here, we couple Cas9 gene editing with quantitative *in vivo* analyses to investigate the functions of
104 individual LBSs within a homotypic cluster. We find that LBS number emerges as a major force in shaping
105 the developmental gradient. The LBS dose modulates both probability and intensity of *sygl-1*
106 transcription, abundance of *sygl-1* mRNA and protein, and size of the GSC pool. Furthermore, we discover
107 that LBSs on separate chromosomes act additively, while LBSs on the same chromosome act
108 synergistically. Finally, we identify rough boundaries for the functional threshold of SYGL-1 abundance
109 that is required for self-renewal. This *in vivo* investigation provides a model approach for learning how
110 DNA *cis*-regulatory elements transform signaling inputs into reproducible patterns of gene expression
111 during development.
112
113 **Results**
114 **A cluster of three *sygl-1* LBSs activate Notch-dependent expression**
115 Four computationally predicted Notch-dependent *cis*-regulatory elements are named LBS A through
116 D (Fig. 1E). LBS B, C and D exist in a cluster while LBS A resides upstream of the cluster. In other
117 *Caenorhabditids*, *sygl-1* 5' flanking regions contain LBS clusters in species-specific patterns containing at
118 least two LBSs (Fig. S1A). LBS B, C, and D sequences adhere to the canonical CSL binding motif, while LBS
119 A lacks the initial pyrimidine and is thus noncanonical. Such noncanonical LBSs compete poorly for CSL

120 binding in gel shift assays (Christensen et al., 1996; Nellesen et al., 1999; Torella et al., 2014; Tun et al.,
121 1994), and are expected to be weaker sites *in vivo*.

122 We hypothesized that the BCD cluster is largely responsible for Notch-dependent regulation of *sygl-1*
123 expression in GSCs. To test this idea, we used Cas9 gene editing to generate two mutants in endogenous
124 *sygl-1* DNA: *A mut* changes 4 basepairs in LBS A, and *BCD mut* changes 5 bp in each of LBS B, C, and D (Fig
125 1E, see Methods mutant design). Both *A mut* and *BCD mut* animals were fertile and their germlines were
126 of normal size and organization in the presence of wild-type *lst-1*, the functionally redundant counterpart
127 of *sygl-1*. However, when *lst-1* was removed, *BCD mut* adults were sterile with a Glp phenotype (loss of
128 GSCs), while *A mut* adults remained fertile with a normal germline. Therefore, *BCD mut* had a dramatic
129 effect on germline development, but *A mut* had no apparent effect. To visualize SYGL-1 protein, we
130 inserted a V5 epitope tag in each mutant (Fig 1E). Initial analyses focused on the distal gonad, where *sygl-*
131 *1* expression is Notch-dependent, and were performed in animals with wild-type *lst-1* to ensure a healthy
132 germline. *A mut* had a wild-type pattern of SYGL-1 protein, both in abundance and distribution, but *BCD*
133 *mut* had no SYGL-1 (Fig. 1F-G). Consistent with the idea that LBSs drive Notch-specific *sygl-1* transcription,
134 the Notch-independent production of SYGL-1 appeared comparable in the proximal germlines of wild-
135 type, *A mut*, and *BCD mut* (Fig. S1B). In an attempt to increase expression, we transformed LBS A to a
136 canonical motif, but found no effect (Fig. S1C-D). We conclude that the BCD cluster is responsible for
137 Notch regulation of SYGL-1 expression in GSCs.

138 To assay functions of individual elements in the BCD cluster, we mutated the sequence of each LBS
139 from the canonical 5' CGTGGGAA 3' motif to 5' TGACGTCA 3' (differences from canonical motif underlined;
140 see Methods). The three LBSs were mutated singly and in all possible pairs (Fig 2A). We then subjected all
141 mutants to a series of molecular and biological assays (Fig 2-5). As a control for the sequence change, we
142 created a distinct LBS D mutant, *alt D mut,* which had effects comparable to *D mut* (Fig. S5). The *sygl-1*
143 LBS single and double mutants were all homozygous fertile in the presence of wild-type *lst-1,* the
144 functionally redundant counterpart of *sygl-1* (Fig. 1A-B). Molecular assays were therefore done with *lst-*
145 *1(+)* to ensure a healthy germline, but stem cell assays were done in an *lst-1(ø)* background. The following
146 sections describe molecular assays first and then biological assays.

147

148 ***sygl-1* LBS mutants fire fewer and weaker active transcription sites**

149 We visualized *sygl-1* RNAs *in situ* with high resolution and spatiotemporal precision using single
150 molecule FISH (smFISH). Fixed gonads were treated with two probe sets that were distinctly labeled to
151 *sygl-1* exons or introns (Fig. 2A). Figure 2B shows representative smFISH images for LBS single and double

152 mutants plus wild-type and *sygl-1(ø)* controls. The *sygl-1* intron probe detected nascent transcripts in the
153 nucleus as bright spots (Fig. 2B, green, left column), while the *sygl-1* exon probe detected both nuclear
154 bright spots and a multitude of dim spots in the cytoplasm (Fig. 2B, middle column, color scaled by
155 intensity). Overlapping exon and intron probe signals in the nucleus identified *sygl-1* active transcription
156 sites (ATS) (Fig. 2B arrowheads), while the dim cytoplasmic spots identified *sygl-1* mRNAs (Fig. 2B, arrows)
157 (see Lee et al. 2016 for additional *sygl-1* ATS and mRNA validation).

158 We quantified effects of LBS mutations on transcription in 3D with a MATLAB code used previously to
159 score wild-type *sygl-1* transcription (Crittenden et al., 2019; Lee et al., 2016). As established in those
160 earlier works, the percentage of cells with any *sygl-1* ATS provides a measure of *sygl-1* transcriptional
161 probability, and the intensity of each ATS signal provides a measure of firing strength. When LBS mutants
162 were scored individually, each single mutant lowered transcription substantially, and each double mutant
163 nearly abolished it (Fig. S2). Because the three LBS single mutants all had similar effects (Fig. S2B,D-E), as
164 did the three double mutants (Fig. S2C,D-E), and because all made far fewer ATS than wild-type (Fig. S2B-
165 E), we pooled ATS data into collective "LBS single mut" and "LBS double mut" datasets (Fig. 2C-F) for
166 further analyses.

167 Transcriptional probability was scored in cells as a function of distance from the distal end of the
168 gonad. For wild-type, probability was highest at the distal end adjacent to the niche and lowered
169 progressively with distance from the end (Fig. 2C), as previously reported (Crittenden et al., 2019; Lee et
170 al., 2016). In LBS single mutants, the probability was lower than wild-type, but similarly graded; in LBS
171 double mutants, the probability was near zero (Fig. 2C, Fig. S2A-C). Overall, transcriptional probabilities
172 were dramatically attenuated in both height and spatial extent along the gonadal axis with LBS double
173 mutants having the most severe effect. As a complementary measure of transcriptional probability, we
174 scored the number of *sygl-1* ATS in each nucleus. Because *sygl-1* transcriptional probability is stochastic
175 and unrelated to cell cycle stage (Lee et al., 2016), any nucleus in the dividing pool of germ cells might
176 possess zero to four *sygl-1* ATS, depending on chromosome replication and probability of *sygl-1*
177 transcription. Consistent with our first measure, the percentage of nuclei with more than one ATS was
178 lower in LBS single mutants than wild-type and even lower in LBS double mutants (Fig. 2D, S2E). Thus, LBS
179 dose regulates the probability of Notch-dependent *sygl-1* transcription.

180 We next scored ATS signal intensity as a metric of transcriptional firing strength. Intensity values from
181 individual ATS were captured in the exon channel and normalized using the average raw intensity of
182 cytoplasmic mRNA (see Methods). When plotted as a function of position along the gonadal axis, mean
183 ATS intensities appeared to decrease further from the distal end (Fig. 2E). To estimate the average number

184 of nascent transcripts at each ATS, we divided the average normalized ATS intensities by the average
185 normalized mRNA intensity (see Methods). By this measure, an ATS in LBS single mutants generated ~20%
186 fewer nascent transcripts than wild-type, on average, and an ATS in LBS double mutants made ~50% fewer
187 transcripts, on average (Fig. 2F). We conclude that *sygl-1* LBS dose regulates both the probability and
188 intensity of *sygl-1* transcription.
189
190 ***sygl-1* LBS single mutants reduce *sygl-1* mRNA and protein subtantially**
191 We analyzed *sygl-1* mRNAs and SYGL-1 protein in all three LBS single mutants to learn how their
192 reduced transcription affects molecular output in the distal gonad. The *sygl-1* mRNAs were quantified
193 from the same smFISH images used for ATS analyses, where LBS mutants were not epitope-tagged. SYGL-
194 1 protein was quantified with immunostaining of a V5 epitope tag inserted at the SYGL-1 C-terminus of
195 each LBS mutant. This V5 tag has no detectable effect on SYGL-1 protein function (Shin et al., 2017).
196 To quantitate *sygl-1* mRNAs, we used MATLAB to detect and count cytoplasmic spots in the exon
197 channel of smFISH images, as described previously (Crittenden et al., 2019; Lee et al., 2016) (see Methods,
198 Fig. S3A). In LBS single mutants, mRNA abundance was reduced to slightly less than half of wild-type (Fig.
199 3A,C), and spatial extents along the gonadal axis were shorter than wild-type by about 5 µm or 1-2 cell
200 rows (Fig. 3A, vertical lines).
201 To quantitate SYGL-1 protein, we stained LBS single mutants with α-V5 antibodies (Fig. S3B) and
202 scored fluorescence intensities along the gonadal axis using FIJI (see Methods). In LBS single mutants, the
203 peaks of the SYGL-1 gradients were reduced to about 40% of wild-type (Fig. 3B,D), and spatial extents
204 were shorter by about 25% of wild-type (~15 µm or 3-5 cell rows) (Fig 3B, vertical lines). We conclude that
205 the gradients of both *sygl-1* RNA and SYGL-1 protein are reduced to a similar degree in all three LBS single
206 mutants.
207
208 ***sygl-1* LBS double mutants nearly eliminate *sygl-1* mRNA and protein**
209 We also quantified *sygl-1* mRNA and SYGL-1 protein in LBS double mutants, using the same strategy
210 as for LBS single mutants. The Notch-dependent *sygl-1* mRNA abundance was below background in the
211 distal-most germ cells in *BD mut* and just above background in *BC mut* and *CD mut* (Fig. 3E, insets) (see
212 Methods). SYGL-1 protein was also very low, but again only *BD mut* lacked distal Notch-dependent signal
213 above background (Fig. 3F, horizontal dashed lines; Fig. S3D). We conclude that protein levels parallel
214 mRNA levels in each of the three *sygl-1* LBS double mutants, which are expressed at or near zero.
215

216 **LBS single but not double mutants make enough SYGL-1 to maintain adult GSCs**

217 The molecular quantitation described above was done in an *lst-1(+)* background to ensure a healthy
218 germline. However, LST-1 masks stem cell defects in *sygl-1* LBS mutants, because of redundancy (Fig. 1B).
219 To score effects of the LBS mutants on stem cell maintenance, we removed LST-1 genetically by
220 introducing *lst-1(ø)* into each mutant. All three LBS single mutants were fertile in an *lst-1(ø)* background
221 and had a germ line of normal size and organization. By contrast, all three LBS double mutants were sterile
222 with tiny sperm-filled germlines, the Glp phenotype (Fig. 4A). Therefore, LBS single mutants generate
223 SYGL-1 at an abundance above the functional threshold required to maintain adult GSCs, but LBS double
224 mutants do not.

225

226 **GSC pool size is reduced in LBS single mutants**

227 Although the LBS single mutants maintain adult GSCs, we suspected that their lower SYGL-1
228 abundance might maintain fewer GSCs and thus shrink GSC pool size. To test this idea, we used three
229 complementary assays (Fig. 4B). All were performed in an *lst-1(ø)* background to eliminate LST-1
230 redundancy. First, we measured progenitor zone (PZ) size, a common proxy for GSC pool size. Both PZ
231 length along the gonadal axis and total PZ cell number were reduced by about half in all three LBS single
232 mutants compared to wild-type (Fig. 4C-D). Second, we measured distribution of GLD-1, a marker of germ
233 cell differentiation. In *lst-1(ø)* control gonads, GLD-1 abundance increased as germ cells move proximally
234 through the progenitor zone (Fig 4E), as previously reported (Brenner and Schedl, 2016; Hansen et al.,
235 2004; Jones et al., 1996). We focused on *D mut* for this and next assay, because the LBS single mutants
236 had behaved similarly overall. In *D mut* gonads the GLD-1 increase shifted distally compared to the control
237 (Fig. 4E, gray arrow). The likely interpretation of the shorter PZs and distally-shifted GLD-1 increase is that
238 germ cells are triggered to begin differentiation more distally in LBS single mutants than controls. Third,
239 we estimated GSC pool size, using the *emb-30* assay. This assay provides a rough but more direct measure
240 than other assays (Fig. 4B, see legend for explanation). When shifted to restrictive temperature, *emb-30*
241 mutants reveal a distal GSC pool and a proximal pool of GSC daughters starting to differentiate (Cinquin
242 et al., 2010). To estimate GSC pool size in an LBS single mutant, we shifted adults to restrictive
243 temperature for 12.5 hours, stained gonads with α-GLD-1 plus a marker of mitosis (α-PH3), and counted
244 undifferentiated GSCs in the distal gonad (see Methods). *D mut* gonads had a visibly smaller GSC pool than
245 the control (Fig. 4F), with 18 cells on average compared to 34 (Fig. 4G). Together, these assays provide
246 complementary lines of evidence that LBS single mutants maintain a smaller-than-normal GSC pool.

247

248 **LBSs have roughly equivalent but not identical activivities**

249 Data in Figures 2-4 support the idea that the three LBS in the *sygl-1* cluster have essentially equivalent
250 roles in regulating *sygl-1* expression and GSC maintenance. Two clues that they might not be identical
251 were that *BC mut* and *CD mut* made marginally more *sygl-1* mRNA and protein than *BD mut* (Fig 3E,F) and
252 that *D mut* had fewer cells in the PZ than *B mut* or *C mut* (Fig. 4D). To investigate these differences in more
253 depth, we turned to LBS double mutants: each leaves one LBS intact and can be used to score activity of
254 that "solo" LBS.

255 To ask if the minor molecular differences among LBS double mutants lead to biological differences,
256 we first measured PZ lengths. LBS double mutants do not have a PZ in an *lst-1(ø)* background, so we used
257 an *lst-1(+)* background for this experiment. LBS double mutants had a shorter-than-normal PZ, similar to
258 *sygl-1(ø)* and consistent with their near-complete elimination of SYGL-1 (Fig. 5A). However, PZ length was
259 marginally shorter in *BD mut* than the other double mutants ($p = 0.04$), which were not different from
260 each other ($p = 0.10$). Because this difference was so slight, we tried another approach. We removed *lst-*
261 *1* genetically and counted total number of germ cells in fourth larval stage (L4) larvae. In control *lst-1(ø)*
262 *sygl-1(ø)* larvae, GSCs begin differentiating in L1 stage (Kershner et al., 2014). Therefore, if L4 larvae have
263 more germ cells than the *lst-1(ø) sygl-1(ø)* control, the solo LBS must have made more SYGL-1 than the
264 null. Germ cells were counted with DAPI and a sperm marker in whole-fixed L4 larvae (see Methods). *BD*
265 *mut* made the same number of germ cells as the control, but the other two LBS double mutants had five-
266 fold more germ cells than the control (Fig. 5B). Therefore, solo LBS B and solo LBS D must each have weak
267 transcriptional activity, at least in larvae, but solo LBS C is equivalent to the null.

268 The detectable biological activities of *BC mut* and *CD mut* made us wonder if the mRNA numbers in
269 Figure 3E, which are averages, might be misleading. A previous work showed that adjacent germ cells can
270 differ dramatically in mRNA number (Lee et al., 2016). Perhaps one or a few cells in LBS double mutants
271 make considerably more than the average and others make none (Fig. 5C). To test this idea, we reassessed
272 *sygl-1* RNA numbers on a cell-by-cell basis in the distal bin (0-5 µm) of wild-type, LBS single mutants, LBS
273 double mutants and *sygl-1(ø)*. Virtually all cells had ≥5 mRNAs in wild-type and most cells had ≥5 mRNAs
274 in LBS single mutants (Fig S4B). By contrast, *BD mut* and *sygl-1(ø)* had virtually no cells with ≥5 mRNAs,
275 but *BC mut* and *CD mut* both had a low percentage of cells with ≥5 mRNAs (Fig 5D). This cell-by-cell analysis
276 reveals differences among the LBS double mutants that bulk measurements missed. Those differences are
277 consistent with the conclusion that solo LBS C is less active than solo LBS B or LBS D.

278

279 **LBS number can function additively**

280 Our initial analyses suggested that LBS number plays a critical role in shaping the *sygl-1* transcriptional
281 gradient: three LBS generated a more abundant and extended gradient than two LBS, while two LBS
282 generated a modest gradient in comparison and one LBS was close to null with no gradient (Figs 2-3). They
283 also suggested that LBS number affects the extent of GSC maintenance. Both PZ size and GSC pool size
284 were larger in wild-type than LBS single mutants, and both were gone in LBS double mutants (Fig 4). To
285 further investigate the role of LBS number in shaping SYGL-1 output, we created animals heterozygous for
286 distinct LBS regulatory regions (see Methods). To score molecular and biological outputs from one set of
287 images, we placed all heterozygotes and all controls in an *lst-1(ø)* background.
288 We first compared *sygl-1* wild-type (*WT*) homozygotes to *WT/BCD mut* heterozygotes. *WT* carries six
289 LBSs, three on each chromosome, whereas *WT/BCD mut* carries only three LBSs, three on the *WT*
290 chromosome and none on the *BCD mut* chromosome. The three LBSs in *WT/BCD mut* produced 65% as
291 much SYGL-1 as the six LBSs in *WT,* a bit more than half (Fig 6A). We next compared *WT* homozygotes
292 with *B mut* homozygotes (four LBSs, two on each chromosome), and *B/BCD mut* heterozygotes (two LBSs,
293 both on the same chromosome). The two LBSs in *B/BCD mut* produced about half as much as the four
294 LBSs in *B mut,* and about a third as much as the six LBSs in *WT* (Fig. 6B). We were intrigued that SYGL-1
295 abundance in *B mut* was more than half of *WT* in *lst-1(ø)*, but less than half of *WT* in *lst-1(+)* (compare Fig
296 6B to Fig 3B). This difference is explained by an effect of *lst-1(ø)* on SYGL-1 expression (Fig S7A-B).
297 Regardless, when all mutants were scored in *lst-1(ø)* (Fig. 6B), LBS number or dose determines the relative
298 SYGL-1 abundance, consistent with findings in *lst-1(+)* (Fig 2,3).
299 We next addressed the question of whether the SYGL-1 level generated in *B/BCD mut* was above or
300 below the threshold for GSC maintenance. This question can only be addressed in a *lst-1(ø)* background
301 where GSC maintenance depends solely on SYGL-1. All strains scored above for SYGL-1 abundance,
302 including *B/BCD mut,* had a normal fertile germline with a PZ and GSCs maintained into adulthood. Thus,
303 *B/BCD mut* makes SYGL-1 at or above the threshold required to maintain GSCs into adulthood.
304 Unexpectedly, PZ sizes were similar in *B mut* with its four LBSs and *B/BCD mut* with its two LBSs (Fig 6C-
305 D). The relationship between SYGL-1 abundance and PZ size must therefore be explored further, perhaps
306 by creating additional LBS mutants that modulate SYGL-1 abundance more finely and analyzing in more
307 depth the circuitry responsible for GSC maintenance.
308
309 **Neighboring LBS within a single cluster act synergistically**
310 Comparison of results from LBS single mutants and LBS double mutants presented a paradox (Fig. 6E).
311 A solo *sygl-1* LBS drove little or no expression in LBS double mutants and had little or no biological activity,

312 but removal of any one LBS reduced expression substantially. For example, solo LBS C had no detectable
313 activity in *BD mut* (Fig. 5B,D), but removal of LBS C in *C mut* had a substantial effect (Figs. 3, 4, S4B). How
314 can an LBS impact *sygl-1* expression so much when mutated on its own, but have no activity when it is the
315 only LBS retained in the cluster? We suggest that LBS synergy between neighboring LBS within a single
316 cluster solves this paradox. In support of this idea, *B/BCD mut* heterozygotes possess only two LBSs, but
317 they reside within the same cluster and make enough SYGL-1 to maintain adult GSCs (Fig. 6B-D). By
318 contrast, *BD mut* homozygotes also possess only two LBSs, a solo LBS C in each cluster, but they are on
319 different chromosomes and cannot maintain GSCs, even in larvae (Fig 5B, Fig 6C-D). Although SYGL-1
320 abundance could not be measured in *BD mut,* because it lacks GSCs and hence a germline tissue, we infer
321 that SYGL-1 abundance in *BD mut* must be below the SYGL-1 threshold and is likely to be comparable to
322 *sygl-1(ø)* (Fig. 5B). We conclude that neighboring LBS on the same chromosome act synergistically.
323
324 **Discussion**
325
326 **Functional analysis of a homotypic CRE cluster in its natural developmental context**
327 Clusters of closely spaced DNA *cis*-regulatory elements are common in animal genomes and point
328 mutations in these elements are critical to evolution and disease (Crocker et al., 2016; Ezer et al., 2014;
329 Gotea et al., 2010; Madani Tonekaboni et al., 2019; Melton et al., 2015; Payne and Wagner, 2015; Stern
330 and Orgogozo, 2009). Traditionally, functional analyses of CREs and CRE clusters have relied on artificial
331 assays, such as reporter transgenes and heterologous cells (e.g. Hardison and Taylor, 2012; Shlyueva et
332 al., 2014), while analyses in their natural context remain largely unexplored. The *C. elegans sygl-1* LBS
333 cluster has several advantages for *in vivo* analyses of CRE function. Rapid Cas9 gene editing in *C. elegans*
334 and ability to freeze strains both facilitate the systematic generation of CRE mutants for comparison. In
335 addition, the relative simplicity of *C. elegans* hits a sweet spot: mechanisms governing nematode
336 transcription are metaozoan but with fewer layers of complexity than mammals. In this work, we
337 investigate a homotypic cluster of three CREs in *sygl-1* regulatory DNA, each with the same conserved
338 sequence. This cluster responds continuously to Notch signaling to drive *sygl-1* transcription and maintain
339 germline stem cells throughout development. As a result, the *sygl-1* gene allows us to directly link LBS
340 function to *sygl-1* transcription and stem cell maintenance. This simple Notch-dependent LBS cluster
341 therefore provides a powerful model to understand how CREs and CRE clusters regulate development in
342 time and space. Given the overwhelming importance of CRE clusters in developmental control and the

343 recent advent of efficient gene editing, analyses of CRE function in a natural *in vivo* context will be an
344 essential facet of future studies.
345
346 **LBS additivity and synergy**
347 A cluster of three closely spaced Notch-dependent CREs, called LBS B – LBS D, drives *sygl-1* expression
348 in the distal gonad. To explore activities of individual LBSs within the cluster, as well as LBS pairs, we
349 generated a set of all possible LBS single, double and triple mutants. The three LBS single mutants reduced
350 *sygl-1* expression dramatically with levels roughly equivalent to each other (Fig. 7A). Therefore, each LBS
351 must be essential for generating the wild-type level of *sygl-1* expression, and the three must be roughly
352 equivalent in activity. A corollary is that the pairs of wild-type LBSs remaining in each LBS single mutant
353 have similar activities, despite differences in spacing and polarity (Fig. 7B). A previous study of a different
354 *C. elegans* Notch-dependent *cis*-regulatory region, analyzed in embryos with a reporter transgene, also
355 found no effect of LBS polarity on response strength (Neves et al., 2007). Thus, LBS activities within the
356 *sygl-1* cluster can tolerate differences in orientation and spacing, though the limits of that tolerance have
357 not been tested.
358 Additional comparisons, including LBS homozygotes and heterozygotes, revealed that LBS activities
359 are additive when on separate chromosomes (Fig 6A,B), but synergistic as neighbors within a single cluster
360 (Fig 3F; Fig 6B-D). Notch-dependent CREs are also synergistic in flies and mammals (Arnett et al., 2010;
361 Bailey and Posakony, 1995; Cave et al., 2005; Nam et al., 2007). Traditionally, CRE synergy is deduced
362 when the transcriptional readout from neighboring CREs is substantially greater than the summed readout
363 of separate CREs (Carey, 1991; Ptashne, 1988). To identify synergy between *C. elegans* LBSs, we compared
364 *sygl-1* expression in animals carrying only two LBSs in *cis,* both on the same chromosome, to *sygl-1*
365 expression in animals carrying only two LBSs in *trans*, one on each chromosome. Two LBSs in *cis* drove
366 expression at a substantially higher level than two LBSs in *trans,* revealing synergy between neighboring
367 LBSs. Indeed, the two LBSs in *cis* made enough SYGL-1 to maintain adult stem cells, whereas the two LBS
368 in *trans* made too little to maintain stem cells. In flies and mammals, a head-to-head polarity of Notch-
369 dependent CREs orients NICD proteins in neighboring transcription factor complexes to interact
370 cooperatively at a molecular interface that has not been conserved in *C. elegans* (see Introduction).
371 Because *C. elegans* LBS polarity is not critical (Neves et al., 2007; this work), it seems unlikely that *C.*
372 *elegans* NICDs interact physically via a different interface. Therefore, we suspect LBS synergy employs a
373 distinct mechanism.

374 One possibility for the molecular basis of LBS synergy in *C. elegans* is that neighboring LBSs enhance
375 LAG-1/CSL occupancy at the cluster. Like many transcription factors, CSL proteins rapidly bind and release
376 sites with dwell times on the order of one or a few seconds (Falo-Sanjuan et al., 2019; Giaimo et al., 2021;
377 Gomez-Lamarca et al., 2018) and yet their transcriptional bursts last for much longer (10 – 70 minutes for
378 *sygl-1*) (Falo-Sanjuan et al., 2019; Lammers et al., 2020; Lee et al., 2019). One can imagine that as LAG-1
379 releases from an LBS, the existence of a neighboring LBS increases its rebinding. This idea is consistent
380 with the increased occupancy of CSL proteins observed upon Notch activation, especially in genes with
381 clusters of binding sites (Castel et al., 2013; Housden et al., 2013; Wang et al., 2014). Another possibility
382 is "assisted loading", where binding of one LAG-1 protein to an LBS indirectly facilitates binding of another,
383 for example by increasing chromatin accessibility and/or increasing the local concentration of other
384 factors that aid LAG-1 recruitment and/or optimize its binding (Ezer et al., 2014; Falo-Sanjuan and Bray,
385 2020). Both possibilities are consistent with our finding that wild-type clusters with three LBSs drive more
386 transcription than mutant clusters with two LBSs and dramatically more than clusters with only one LBS.
387 They are also consistent with the finding that three neighboring LBSs on the wild-type chromosome in
388 *WT/BCD mut* make as much SYGL-1 as two neighboring LBSs on each of the clusters in *B mut,* even though
389 *WT/BCD mut* possesses one fewer LBS than *B mut* (three versus four) (Fig. 6A,B). Thus, both LBS number
390 and neighborhood are important to activity level. An important question for the future is whether LBS
391 mutants lead to differences in duration or frequency of *sygl-1* transcriptional bursts. Regardless, we
392 suggest that the combination of LBS additivity and synergy reported here may apply to homotypic CRE
393 clusters more broadly.
394
395 **SYGL-1 extent governs threshold for GSC self-renewal**
396 An attractive concept is that the extent of SYGL-1 expression along the gonadal axis determines the
397 size of the GSC pool (reviewed in Hubbard and Schedl, 2019). According to this model, GSCs self-renew
398 in the presence of SYGL-1, but begin to differentiate upon its loss. This idea was proposed from the finding
399 that expansion of the SYGL-1 gradient enlarges the GSC pool or can even form a tumor, depending on
400 extent of the expansion (Shin et al., 2017). However, the effect of a smaller than normal SYGL-1 gradient
401 had not been explored, because only *sygl-1* null mutants were available prior to this work. This work
402 generates LBS mutants, which shrink the SYGL-1 gradient but do not abolish it. These mutants make
403 enough SYGL-1 to maintain GSCs without its redundant counterpart LST-1, but they also reduce GSC pool
404 size by about half. Therefore, an increase in SYGL-1 enlarges the pool (Shin et al., 2017), and a decrease

405 in SYGL-1 shrinks it (this work). Together, these results show definitively that the extent of SYGL-1
406 expression along the gonadal axis determines GSC pool size.
407 GSCs are maintained where the SYGL-1 gradient is at its peak, and their daughters begin to
408 differentiate where the gradient becomes too low. But how much SYGL-1 is sufficient to promote self-
409 renewal and how low must SYGL-1 be to trigger differentiation? To gain insight, we measured SYGL-1
410 abundance in the absence of LST-1, the redundant counterpart of SYGL-1. When LST-1 is wild-type, stem
411 cells can use either SYGL-1 or LST-1, effectively masking effects of varying SYGL-1 levels. However when
412 LST-1 is removed, SYGL-1 alone is responsible for GSC maintenance. So the correlation between SYGL-1
413 abundance and stem cell maintenance was assayed in an *lst-1(ø)* background. We found that LBS single
414 mutants and *WT/BCD mut* and *B/BCD mut* heterozygotes all made enough SYGL-1 to maintain adult stem
415 cells and were thus above the threshold. By contrast, LBS double mutants made too little SYGL-1 to
416 maintain adult stem cells and were thus below the threshold. Therefore, the SYGL-1 functional threshold
417 is ≤40% of wild-type SYGL-1 abundance (Fig 6B). However, this number is based on measurements made
418 in *lst-1(ø)* germlines and cannot be translated simply to *lst-1(+)* germlines (Fig S7).
419
420 **Future directions**
421 This work manipulates CREs to tune the abundance of one crucial stem cell self-renewal regulator. A
422 long term goal for comprehensive understanding of the decision to self-renew or differentiate will be to
423 integrate cell-autonomous factors (e.g. abundance ratios between critical stem cell regulators like SYGL-
424 1, LST-1 and their regulators) and non-cell-autonomous factors (e.g. mechanical force from tissue
425 morphology, altered signaling in aged animals, the extracellular matrix, soma-germline communication)
426 (Chacon-Martinez et al., 2018; Lin et al., 2020; Muncie and Weaver, 2018; Perez-Gonzalez et al., 2021;
427 Starich and Greenstein, 2020). Untangling the relative contributions of these factors is a next challenge to
428 improve predictive models and stem cell therapies. This work modulates SYGL-1 abundance using LBS
429 manipulations and lays a foundation in a tractable model organism to test a variety of genetic and
430 environmental contexts and begin to tease apart these critical ratios and relationships.
431
432 **Acknowledgements**
433 The authors thank David Wassarman and members of the Kimble and Wickens labs for helpful discussions
434 throughout the course of this work. We thank Jane Selegue, Peggy Kroll-Conner, and Hannah Moulton for
435 assistance with experiments or strain building. We thank Ahlan Ferdous, Sarah Crittenden, Melissa
436 Harrison and David Wassarman for critical comments on the manuscript. Thanks to Sam Engle and the

UW-Madison CALS Statistical Consulting Lab for discussions on statistics. TRL was supported by the NSF; this material is based upon work supported by the National Science Foundation Graduate Research Fellowship under Grant No. DGE-1747503. Any opinions, findings, and conclusions or recommendations expressed in this material are those of the authors and do not reflect the views of the National Science Foundation. JK was an Investigator of the Howard Hughes Medical Institute and is now supported by NIH R01 GM134119.

Author contributions

TRL conceived and performed experiments, analyzed data, and wrote the paper. MX and CC performed experiments and analyzed data. CHL analyzed data. JK conceived experiments and wrote the paper.

Competing interests: The authors declare no competing interests.

Methods

C. elegans strains and nomenclature

See Table S1 for a list of genotypes and the figures each strain was used in. "*ø*" refers to null mutants that have a CRISPR deletion of the coding region; "*+*" refers to a wild-type copy of the gene. For simplicity, several different genotypes may be referred to using the same in-text abbreviation (e.g. "*D mut*" can refer to *lst-1(ø) sygl-1::V5(D mut), lst-1(ø) sygl-1(D mut), sygl-1(D mut)*, or *lst-1(ø) sygl-1::V5(D mut); emb-30(tn377)*). All strains were maintained at 20°C unless noted, using standard culture techniques (Brenner, 1974). The balancer used for *LG I* was *hT2[qIs48]* (Siegfried and Kimble, 2002).

CRISPR/Cas9 gene editing

No transgenes were used; all genetic edits were done by CRISPR/Cas9 genome editing at the endogenous loci. Recombinant Cas9 protein (Paix et al., 2015), single-stranded DNA oligo repair templates complementary to the nontarget strand (Richardson et al., 2016), and custom crRNAs and tracrRNA (Integrated DNA Technologies) were injected into the *C. elegans* germline. A co-conversion approach was used (Arribere et al., 2014): single-stranded DNA repair templates and crRNAs were designed against both the *sygl-1* mutation of interest and a *dpy-10* co-injection marker. Edits of the *dpy-10* co-injection marker create visible phenotypes, decreasing the number of animals that must be screened for the desired *sygl-1* edit by PCR. The *dpy-10* repair and crRNA sequences are from the Fire Lab (repair: 5'

469 CACTTGAACTTCAATACGGCAAGATGAGAATGACTGGAAACCGTACCGCATGCGGTGCCTATGGTAGCGGAGCTT
470 CACATGGCTTCAGACCAACAGCCTAT 3'; crRNA: 5' GCTACCATAGGCACCACGAG 3'). Final concentrations in
471 the injection mix are as follows: *dpy-10* repair 1.34 µm; *dpy-10* crRNA 4 µm; gene-specific repair 4 µm;
472 gene-specific crRNA 9.6 µm; tracrRNA 13.6 µm; recombinant Cas9 protein 25 µm).

473 *Scarless CRISPR/Cas9 genome editing*

474 To create a canonical LBS A motif (Fig S1C-D), we followed a two-step CRISPR-Cas9 editing protocol
475 which in the first step creates the point mutation and replaces a stretch of 23 nt in the *sygl-1* 5' flanking
476 sequence with *dpy-10* protospacer sequence; the second step removes the *dpy-10* sequence to create a
477 scarless edit (El Mouridi et al., 2017). After completing the first step of this protocol, we found that
478 mutating LBS A to a canonical LBS produced SYGL-1 at levels similar to wild-type and abandoned the
479 second step.

480

481 **Design of LBS mutation**

482 Both the 5' TGACGTCA 3' and 5' GGATCCAA 3' LBS mutations were designed to mimic LBS mutations
483 from the literature where loss of function had been demonstrated (Choi et al., 2013; Christensen et al.,
484 1996; Kershner et al., 2014; Neves et al., 2007; Yoo et al., 2004). Mutating the endogenous LBSs presented
485 a genotyping challenge in that the nucleotides in the LBS mutation are the only change from wild-type.
486 Thus, we mutated five nucleotides and designed mutant sequences that add a restriction enzyme cleavage
487 site (*AatII* for 5' TGACGTCA 3' and *BamHI* for 5' GGATCCAA 3'). Additionally, LBS mutation disrupts the
488 PAM sequence. We alternatively found that designing PCR primers whose 3' ends overlapped with the
489 mutated five nucleotides successfully generated mutant-specific or wild-type-specific PCR product.

490

491 ***sygl-1* gene diagrams**

492 In Figure 2A, we show a predicted transcription start site (TSS); this TSS was drawn using the
493 Wormbase version WS280 annotation and RNA seq data.

494 Gene diagrams of *sygl-1* are all drawn to scale except that smFISH probes in Fig 2A are drawn larger
495 than to scale for visibility; the center of each line indicates the 5' end of each 20nt-long smFISH probe.

496

497 **Immunostaining**

498 *General staining protocol*

499 Immunostaining was performed as described by the solution extrusion method in Crittenden et al.,
500 2017 with minor modifications. Specific protocol adaptations are listed in sections below. Unless

501 otherwise noted, animals were dissected at L4 + 24 hours at 20°C in a glass petri dish with ~10 mL of
502 PBSTw+0.25 mM levamisole. Samples were moved to a 1.5 mL Eppi tube, fixed in paraformaldehyde
503 (Thermo 28908), washed in 1mL PBSTw, then permeabilized and washed briefly three times in PBSTw
504 before blocking in PBSTw+0.5% BSA (PBSB) for at least 30 minutes at room temperature. Samples were
505 incubated in the primary antibody solution at 4°C overnight, then washed 3-4 times in 1 mL PBSTw before
506 adding 100-200 µL of secondary antibody solution. Samples were incubated in the dark at room
507 temperature for 1 hour. Another series of 3-4 PBSTw washes was repeated, shielding samples from light,
508 then samples were mounted in ProLong Gold antifade reagent (Fisher P36930) on glass slides (FisherFinest
509 Premium 12-544-1) with 22x22 mm coverslips (Azer Scientific ES0107052) and cured in a dark drawer at
510 room temperature prior to imaging (cure times overnight to several days).

511 *V5 epitope tag staining*

512 Fixation: 3% paraformaldehyde for 20 minutes; permeabilization: 0.5% triton in PBS for 5 min; Mouse
513 anti-V5 antibody (SV5-Pk1, Bio-Rad, MCA1360, 1 mg/mL, Dunn et al. *J Immunol methods* 1999) was diluted
514 1:1000 in PBSB; Secondary antibody solution: 0.1 µg/mL DAPI + Donkey anti-Mouse Alexa 555 (1:1000,
515 Thermo Fisher Scientific A31570, lot 1117032); antibody solutions were removed with two quick (10
516 inversions of tube) and two long (10-15 min on rocker) washes. Mounted in 12 µL ProLong Gold Antifade
517 (Thermo Fisher Scientific P36930 or P10144). Note: the α-V5 antibody non-specifically stains the distal tip
518 cell body.

519 *GLD-1 and PH3 staining*

520 The same staining protocol was used for GLD-1 staining (Fig 4E) and *emb-30* assay (Fig 4F-G) except
521 that in the *emb-30* assay animals were maintained at different temperatures and staged differently (see
522 *emb-30* assay). Note: Fig 4B cartoon GLD-1 staining is a representation of wild-type animals, not the *lst-*
523 *1(ø)* control animals. This work is consistent with previously published GLD-1 staining in *lst-1* null animals;
524 GLD-1 is brighter in the distalmost region and shifted distally compared to wild-type (Brenner and Schedl
525 et al. 2016).

526 Fixation: 4% paraformaldehyde for 10 minutes; permeabilization: 0.5% triton in PBSTw+0.5%BSA
527 (PBSB) for 10 minutes; Rabbit anti-GLD-1 (Schedl Lab, Jones et al., 1996) was diluted 1:200 in PBSB; Mouse
528 anti-Phospho-Histone H3 (Ser10) (Cell signaling 9706L, lot 10) was diluted 1:200 in PBSB. Secondary
529 antibody solution: 0.1 µg/mL DAPI and Donkey anti-Rabbit Alexa 647 (Invitrogen Molecular Probes
530 A31571 lot 1252811), Donkey anti-Mouse Alexa 488 (Invitrogen Molecular Probes A21202 lot 1226927).
531 Antibody solutions were removed with two quick (10 inversions of tube) and one long (15 min) wash.
532 Mounted in 18 µL ProLong Glass (Fisher, P36984)

533 *Immunostaining for progenitor zone analysis*

534 For progenitor zone size counts, a similar protocol as above was used except animals were fixed for
535 15 min in 2% paraformaldehyde, permeabilized 15 minutes in 0.5% triton, blocked for 30+ minutes, and
536 stained with mouse anti-DAO-5 1:100 (DSHB, Hadwiger et al., 2010). Some progenitor zone length counts
537 used a shortened method of the above protocol: fixation for 10 minutes in 4% paraformaldehyde + PBSTw,
538 followed by one quick PBSTw wash, 5 minute permeabilization in 0.1% triton+PBS, then one wash in
539 PBSTw and mounted in Vectashield + DAPI (Vector Labs, H-1200).

540 *Image Acquisition*

541 Images were captured on a Leica SP8 confocal microscope. Gonads were imaged from top to bottom
542 with a z slice depth of 0.5 µm. Channels were acquired sequentially (between stacks). α-V5 signal was
543 excited at 561 nm (0.5%, HeNe) and signal was acquired from 564-615 nm (gain 70) with 16 line averages
544 and 2 frame accumulations using a 63x objective at 150% zoom and an 8000 Hz scan head; α-GLD-1 signal
545 was excited at 633 nm (0.2%) and acquired from 564-614 nm (gain 70, 2 line averages) using a 40x
546 objective and 125% zoom or a 63x objective and 100% zoom and a 400 Hz scan head; α-PH3 signal was
547 excited with 561 nm (0.15%, Argon at 25% 24W) and collected from 642-693 nm (gain 80, 1 line average)
548 using a 63x objective and 100% zoom and a 400 Hz scan head; DAPI was excited at 405 nm (0.8-1.2%, UV)
549 and signal acquired from 412-508 nm (gain 500-700).

550

551 **Fluorescence quantitation**

552 FIJI (FIJI Is Just ImageJ) was used to quantitate fluorescence pixel intensities. Workflow is as described
553 in Haupt et al. 2019 and Brenner et al. 2016. A FIJI macro was written to automatically create sum Z
554 projections and save the output as TIFFs. A 50-pixel wide freehand line was drawn from the DTC down the
555 germline image. FIJI Plot Profile tool was used to copy pixel intensity data and paste into Microsoft Excel.

556 *Background subtraction*

557 In Microsoft Excel, an average pixel intensity for each genotype was created by averaging values from
558 individual germlines at each x coordinate. Then, the average pixel intensity per genotype was background
559 subtracted using the average pixel intensity from the negative control (untagged) sample; the exception
560 is Figure 1, where the untagged JK5622 *sygl-1(q828)* control values are not subtracted in order to display
561 them in comparison to *BCD mut* values. For all other experiments, the untagged control was N2 (wild-
562 type).

563 *Normalization of background-subtracted pixel intensities*

564 After pixel intensities were processed as above, intensities were normalized in one of two ways. For
565 Figures 1 and 3, the values at each x coordinate were divided by the maximum intensity from the positive
566 control to transform intensities into a percent of control.
567 For the GLD-1 data in Fig 4E, processed pixel intensities were normalized against an internal control:
568 JK4864 (Table S1) worms expressing a GFP reporter in somatic cells were grown on the same plates and
569 dissected in the same dish as the test worms. The JK4864 control worms have normal GLD-1 expression
570 and the peak value in the JK4864 data was set to 1.0 for each slide.
571 *SEM shading on plots*
572 The SEM values were calculated on background-subtracted pixel intensity values; values from
573 different experiments were averaged together and then normalized. Standard error was calculated using
574 the number of experiments as n. Thus, the SEM shading reflects the spread of pixel intensity values on
575 different slides imaged on different days.
576 SEM shading was used on immunostaining data for some figures but not others. For SYGL-1
577 abundance figures lacking SEM shading, we normalized background-subtracted values to their respective
578 controls (stained in parallel) before averaging together values from different replicates, which makes
579 mean values robust against day-to-day variation in pixel intensity.
580 *Total protein (area under the curve)*
581 To calculate total protein quantitation (Fig 3D), arrays X (distance values in µm) and Y (normalized
582 SYGL-1 intensity values) were imported into MATLAB version R2015a and the command trapz(X,Y) was
583 used to calculate area under the curve.
584 *Measurements along gonadal axis*
585 Microns were converted to germ cell diameters (gcd) using a conversion factor of 3.7 µm/gcd, which
586 was calculated by manually measuring cell diameters in FIJI (10 cells were measured for 1 randomly
587 chosen image from each experiment, using both protein staining and smFISH experiments).
588
589 **Single molecule RNA FISH (smFISH)**
590 The same *sygl*-1 exon and intron probes were used as described in Lee et al, 2016. See also a published
591 smFISH protocol (Lee et al., 2017). Briefly, mid-L4 stage animals were grown on OP50 at 20°C for 24 hours,
592 then dissected as described in Immunostaining. Animals were fixed in 3.7% formaldehyde (37%
593 formaldehyde Amresco, 0493-500ML) for 15-25 minutes and permeabilized in RNAse-free PBS (Fisher
594 BP24384) + 0.1% triton for 10-12 minutes. After an overnight incubation in 70% ethanol (diluted with DEP-
595 C-treated H2O (Ambion AM9922), samples were equilibrated in smFISH wash buffer for 15-20 minutes,

596 then incubated in hybridization buffer plus smFISH probe at 37°C for 46-48 hours. Lyophilized smFISH
597 probes were resuspended in RNAse-free TE buffer (10 mM Tris-HCl, 1 mM EDTA, pH 8.0) to make a 250
598 µM stock solution. The *sygl-1* exon-specific probe set includes 31 unique oligonucleotides labeled with
599 CAL Fluor Red 610 and was used at a final concentration of 0.25 µM. The *sygl-1* intron-specific probe set
600 includes 48 unique oligonucleotides tagged with Quasar 570 and was used at a final concentration of 0.50
601 µM. Samples hybridized at 37°C overnight, then were washed with smFISH wash buffer and 1µg/uL DAPI
602 at 37°C for 40-50 minutes. Finally, samples were resuspended in 12 µL Prolong Gold antifade reagent
603 (Fisher P36930), mounted on glass slides, and cured unsealed in a dark drawer for at least 24 hours to
604 several days before imaging.

605 *Image acquisition settings*

606 Images were captured on a Leica SP8 confocal microscope with the same hardware and Leica software
607 as described in Lee et al., 2016. Gonads were imaged from top to bottom with a z slice depth of 0.3 µm,
608 with a 63x objective at 300% zoom. Channels were acquired sequentially in the following order: *sygl-1*
609 intron Q570 probe was excited at 561 nm (3%, HeNe) and signal was acquired from 564-588 nm (gain 40);
610 *sygl-1* exon C610 probe was excited at 594 nm (3%, DPSS) and signal acquired from 600-680 nm (gain 40);
611 DAPI was excited at 405 nm (0.8-1.2%, UV) and signal acquired from 412-508 nm (gain 500-700). Six of
612 nine experiments were imaged between frames with a 400 Hz scan head and line average of 6 for both
613 RNA channels or 3 for DAPI; three of nine experiments were imaged between stacks with an 8000 Hz scan
614 head and line average of 16 for intron, 32 for exon, and 8 for DAPI with 2 frame accumulations on each
615 channel.

616 *Representative images*

617 Image contrast was adjusted in FIJI equivalently for all main images and for all insets. Contrasts for
618 intron channel differ between main images and insets to highlight ATS number in main images and ATS
619 intensity in insets. Exon channel is pseudo-colored with FIJI default Fire LUT to show cytoplasmic mRNA
620 without saturating ATS. All gonad images were taken from the same experiment.

621

622 **MATLAB analysis of smFISH data**

623 *Removal of data points*

624 Some images in a few experiments displayed bright, nonspecific signal outside the gonad tissue that
625 interfered with detection. Images where the nonspecific signal was greater than 8 um^2 were removed (1
626 *wt*, 10 *C mut*, 6 *D mut*, 3 *CD mut*, 1 *sygl-1(ø)*). Additionally, a small number of images threw errors in
627 MATLAB related to reading the image files (e.g. nuclei imaged too close to edge of frame) and were also

628 removed (5 *C mut*, 5 *BD mut*, 3 *CD mut*, 1 *sygl-1(ø)*). Total number of images quantified are reported in
629 Fig S2E.

630 *MATLAB code*

631 For MATLAB code analysis, refer to Lee et al., 2016, Crittenden et al., 2019. Code modifications
632 described in Crittenden et al., 2019 were also applied to this work. Threshold values were set as 1.0
633 thresForIntron and 0.55 thresForExon for all images. To define cell boundaries for #mRNA/cell
634 calculations, a Voronoi with 3 µm limit was used (the same as in Crittenden et al. 2019 and Lee et al. 2016;
635 does not include center of rachis).

636 *Cytoplasmic spots versus mRNA*

637 The dim cytoplasmic spots range slightly in intensity and size. For *wt* and each LBS mutant, ~60% of
638 cytoplasmic spots have a dim intensity distribution with a low coefficient of variation, consistent with a
639 single mRNA (Fig S3A) (see also Lee et al., 2016). Approximately 1/3 of the cytoplasmic spots in each
640 genotype are a bit larger and their intensity values are approximately twice that of the single mRNA
641 population, consistent with two mRNAs. Rare spots have ≥3 mRNA per cytoplasmic spot. Where possible,
642 number of mRNA are reported rather than the number of cytoplasmic spots, but the #mRNA/cell values
643 represented in Fig 3B, 3E, 5D and S4B are the number of cytoplasmic spots.

644 *Background level and extent of sygl-1 mRNA gradient*

645 The background level in Figures 3B and 3E is 0.956 cytoplasmic spots (or ~1.25 mRNA). This
646 background was determined by calculating one standard deviation above the mean number of
647 cytoplasmic spots detected in the 45-50 µm region of *sygl-1(ø)* control gonads. Local minimums indicate
648 the end of the Notch-dependent *sygl-1* gradient because the slight increase in RNA in the 40-60 µm region
649 is consistent with the rise in proximal Notch-independent *sygl-1* expression.

650 *Normalization of ATS pixel intensities*

651 To control for image-to-image intensity changes, raw exon channel ATS values from each gonad are
652 divided by the mean intensity for the raw single mRNA population (the population of cytoplasmic spots
653 estimated to be one mRNA) within the same gonad. Then, the mean of all the single mRNAs is transformed
654 to 10. Thus, a normalized ATS intensity of 50 was five times brighter than the mRNA within the same
655 image. Normalized ATS intensities were divided by 10 to estimate the number of nascent transcripts per
656 ATS (Fig 2F).

657 *Number of ATS per nucleus pie charts (Fig. 2D)*

658 The percentages of nuclei containing x number of ATS were calculated individually for each
659 experiment. The percentages in the pie charts are the average percent of all the experiments in the

660 datasets. For example, the LBS double mutant dataset contains 94 nuclei and only one of those nuclei
661 contains 3 ATS. That 3-ATS nucleus came from one experiment with 21 total nuclei; that experiment's 3-
662 ATS percentage is 4.8%. The other 7 experiments that contained any ATS-positive nuclei had 0% nuclei
663 with 3 ATS and thus the overall average is 0.6%.

664 *Summary of sygl-1 mRNA data (Fig 3D)*

665 The total number of single mRNAs per experiment was divided by the number of gonads in that
666 experiment; standard deviation was calculated between experimental averages. The peak number of
667 mRNA is the maximum number of cytoplasmic spots detected (bar height in 0-5 µm bin of ave #mRNA/cell
668 plots) as a ratio to WT; standard deviations were calculated between the average values for each
669 independent experiment. Total # mRNA: Ave # mRNA as described above as a ratio to WT.

670

671 **Germline function**

672 *Percent fertile*

673 To score percent fertile, F1 homozygous L4s were picked from balanced LBS single mutant stocks onto
674 a fresh plate. 24 and 48 hours later, one L4+24 or L4+48 adult was singled onto a plate to lay embryos for
675 1.5-3.5 hours. Percent fertility of F2 homozygotes was scored (gravid or not fertile) at low magnification
676 on a Zeiss Discovery.V12 microscope four days after eggs laid. Progeny from a total of eight different
677 adults per genotype were scored. LBS double mutant animals were maintained for many generations and
678 a gravid homozygous animal was never seen. Additionally, *lst-1(ø) sygl-1(LBS double mut)* homozygous
679 L4s were raised at 15° C, 20° C, and 25°C and failed to produce embryos at all temperatures.

680 *Percent Glp*

681 To score percent Glp (germline proliferation abnormal), L4 + 24hr LBS double mutant adults were
682 assessed at high magnification on a Zeiss Axio Imager.D1 microscope by DIC. Sperm were observed at the
683 distal tip of all LBS double mutant germlines at 20° C. LBS single mutants are 0% Glp because 100% of
684 germlines have a progenitor zone.

685

686 **Progenitor zone size**

687 Progenitor zone size was assessed in animals grown at 20°C for 24 hours past mid-L4. Gonads were
688 extruded, fixed, and stained with DAPI or DAPI and α-DAO-5 antibodies (see Immunostaining).

689 *Progenitor zone length*

690 PZ lengths were determined as follows: first, the DTC was located, then the number of cell rows
691 between the DTC and the first crescent were counted. Both sides of the germline were counted and

692 averaged together for one PZ length per germline. Note that because a curved metaphase plate can look
693 similar to a crescent cell, the definition of "first crescent" cell included a requirement for multiple nearby
694 crescent cells. For more information on identifying and scoring PZ, see (Crittenden et al., 2017). Gonads
695 were visualized on a computer monitor for ease of manual counting; µManager software (a plugin for
696 ImageJ) was used to connect the camera and computer (Edelstein et al., 2010).

697 *Number of cells in progenitor zone*

698 A protocol using Imaris software was modified from (Braude et al., 2015; Gopal et al., 2017; Sadeghi
699 et al., 2014). A surface was drawn to mask the PZ region using the drawing contour mode with 1.7 um
700 vertex spacing. The PZ boundary along the gonadal axis was chosen by eye on a middle slice where the
701 first crescent cells could be seen, then the outline was copy/pasted to the first and last slices to create a
702 3D surface. The surface was used to mask the DAO-5 channel. A spots function with an estimated XY
703 diameter of 2.0 um was created in the masked DAO-5 channel. The number of spots was filtered with a
704 quality filter and the threshold was set by moving the slider until no spots were detected outside the
705 germline. Detection was briefly visually checked and the number of spots detected was recorded as the
706 number of cells in the PZ. We also used Imaris to count the number of cells in the PZ for some experiments
707 that were DAPI stained but not DAO-5 stained (Fig S5A-B, Fig 7E). The protocol is the same except we used
708 a 2.7 estimated XY diameter on a masked DAPI channel and spent more time per gonad checking and
709 editing detected spots.

710 Imaris version 9.3.1 was used on a Dell Precision 5820 with 64-bit Windows 10 Education operating
711 system, an Intel® Xeon® W-1245 CPU @3.70GHz processor, and 128 GB of RAM. Leica .lif images were
712 converted to .ims images using Imaris FileConverter v9.5.0.

713

714 **Sperm counts**

715 Mid-L4 larvae were harvested and whole-mount stained with the reduction/oxidation method (Finney
716 and Ruvkun, 1990). Samples were fixed in Ruvkun fixation buffer with 1% paraformaldehyde for 30
717 minutes, followed by disulfide linkage reduction and incubation in blocking solution [1X PBS with 1%
718 bovine serum albumin, 0.5% Triton X-100, 1mM EDTA] for 40 minutes. Samples were then incubated
719 overnight at 4°C with rabbit α-SP56 (1:200, Ward et al. 1986) in blocking solution. Secondary antibody
720 Alexa 555 Goat anti-rabbit (1:1000, Invitrogen Molecular Probes A21429, lot 1246456) was diluted in
721 blocking solution and incubated with samples for at least 2 hours. Samples were washed with blocking
722 solution and 1ng/µL DAPI for 15 minutes, then mounted in Vectashield (#H1000; Vector Laboratories,
723 Burlingame, CA) for visualization with fluorescent compound microscopy.

724 *Calculation of germ cell number*

725 Germlines lacking both *lst-1* and *sygl-1* begin precociously differentiating in L1, two full larval stages
726 earlier than L4, and have completed both spermatogenic meiotic divisions by L3, which creates 16-32
727 sperm from a total of 4-8 germ cells (Kershner et al., 2014). The distalmost cells were scored as
728 undifferentiated by DAPI morphology or as differentiating (either sperm by DAPI morphology and SP56+
729 staining or meiotic by DAPI morphology). Estimates of the number of germ cells were extrapolated as
730 follows: ¼ GSC per sperm, ½ GSC per secondary spermatocyte, and 1 GSC per primary spermatocyte or
731 meiotic cell. Sperm and spermatocytes were counted in one gonad arm in JK5911 and JK6180 and
732 multiplied by two. Sperm were counted in both gonad arms in JK6165 and JK6401.

733

734 **Creating *sygl-1* heterozygotes**

735 LBS mutant/null heterozygotes were created by mating males of an LBS mutant with *sygl-1* null
736 hermaphrodites. Heterozygote cross progeny were assayed by staining for α-V5: SYGL-1 protein is quicker
737 to image and quantify than *sygl-1* mRNA, and LBS effects on SYGL-1 protein abundance were similar to
738 those on *sygl-1* RNA abundance. *BCD mut* was chosen as the *sygl-1* null allele rather than *sygl-1(ø)* (Fig
739 S6A-C). All heterozygotes were created in an *lst-1(ø)* background: SYGL-1 minimum threshold is best
740 defined in *lst-1(ø)*; GSC maintenance and SYGL-1 abundance could be tested in parallel; absence of *lst-1*
741 allowed reliable detection of cross progeny (see below).

742 *Reliably distinguishing cross progeny*

743 Hermaphrodite parents in the heterozygote crosses throw 100% sterile progeny. Therefore, any
744 progeny that maintain GSCs as adults must be heterozygote cross progeny. Only a small percent of
745 progeny on successful mating plates were sterile, which is consistent with the idea that all sterile progeny
746 are self-fertilized progeny from mother hermaphrodites. However, we decided to additionally rule out the
747 possibility that some cross progeny are sterile by using a recessive *rol-6(e187)* allele: only self-fertilized
748 progeny display a Roller phenotype. Thus, heterozygous cross progeny were additionally distinguished as
749 wild-type movers. We repeated a heterozygous cross three times and found that 100% of wild-type mover
750 progeny maintained GSCs; we concluded that it is unlikely the heterozygous cross progeny population
751 includes any sterile animals. After this proof of principle, we assumed that sterile Glp animals were self
752 progeny for all other heterozygous crosses due to technical practicalities.

753 *Strains mated for crosses (see also Table S1)*

754 In Figure 6B-D, *B/BCD mut* are progeny from JK6517 males mated with JK6600 hermaphrodites. In
755 Figure 6A, *WT/BCD mut* are progeny from JK6431 males mated with JK6600 hermaphrodites. In Fig. S6B,

756 *WT/ø* are progeny from JK6431 males mated with JK6401 hermaphrodites. In Figure 6A-D and Fig S6,
757 control animals were also progeny from a male x hermaphrodite cross (e.g. *B mut* in Fig. 6B are progeny
758 from JK6517 males mated with JK6517 hermaphrodites).
759
760 ***emb-30* assay for number of germline stem cells**
761 The *emb-30* assay to estimate the naïve GSC pool size was done as previously described (Cinquin et
762 al. 2010). Animals with *emb-30(ts)* alleles were grown at 15°C permissive temperature until 36 hours past
763 L4, then shifted to 25°C restrictive temperature for 12.5 hours. Temperature shifts were done in a
764 programmable incubator (Echotherm IN35, Torrey Pines Scientific). Gonads were dissected, fixed, and
765 stained for GLD-1, PH3, and DAPI (see Immunostaining). The number of naïve GSCs was estimated by using
766 the multi-point tool in FIJI (Schindelin et al., 2012) to count the number of nuclei distal to the GLD-1
767 staining boundary that were positive for PH3 signal and/or mitotic by DAPI.
768 *Selection of data for analysis*
769 Six of 17 control *lst-1(ø) sygl-1::V5(D mut); emb-30* gonads, kept at permissive temperature, were
770 meiotic. None of the animals in the *lst-1(ø) sygl-1::V5(wt); emb-30* controls (permissive and restrictive)
771 were meiotic, so we interpreted this as a consequence of the mutant *emb-30* background and discarded
772 all meiotic gonads (5/21 for *D mut*, 0/28 for *wt*) from analysis. As established in previously published *emb-*
773 *30* counts (Crittenden et al., 2019), temperature-shifted gonads where most germ cell nuclei were
774 fragmented (4/21 for D mut, 2/28 for WT) were also excluded due to unreliable counting.
775
776 **Descriptors of gradient shape**
777 Values for Figure 7A summary were calculated by averaging together the individual *B mut*, *C mut*, and
778 *D mut* values. We did so because when we consider all factors (e.g. directness of comparison in
779 experimental design, consistency across multiple assays), our clearest conclusions tended to focus on
780 similarities rather than differences between individual LBS single mutants. When we took the same factors
781 into account for LBS double mutants, we found that strong conclusions extended to a clear distinction
782 between *BD mut* and the other two LBS double mutants.
783 *Calculation of a summary LBS single mutant gradient*
784 Primary transcript values are as follows: abundance at peak values from % cells with *sygl-1* ATS Fig 2C
785 graphs (LBS mut: 14.2 ± 5%; WT: 51.8 ± 8%); extent values from Fig 2C graph vertical dashed lines (LBS
786 mut: 15 µm; WT: 25 µm); sum values are an estimate of the total number of primary transcripts per gonad
787 using numbers from Fig S2E (LBS mut: 5.8 ± 4.1 ATS/gonad * 4.5 ± 0.6 tx/ATS = 17 tx/gonad; WT: 24 ± 8.5

ATS/gonad * 5.6 ± 0.5 tx/ATS = 134 tx/gonad). The mRNA values are: abundance from Fig 3A,C (LBS mut: 29 ± 3 mRNA at peak; WT: 62 ± 5 mRNA at peak); extent from Fig 3A (LBS mut: 30 µm; WT: 35 µm); sum from Fig 3C (LBS mut: 2616 ± 864 mRNA; WT: 6274 ± 1478 mRNA). The protein values are: abundance from Fig 3D (LBS mut: 42 ± 13% of WT peak); extent from Fig 3B (LBS mut: 43 µm; WT: 52 µm); sum from Fig 3D (LBS mut: 11557 ± 3678 a.u.; WT: 2781 ± 5739).

Statistics

Box plots

Box plots were generated with the BoxPlotR web tool (Spitzer et al., 2014). BoxPlotR conventions: box limit: 25th and 75th percentiles; whiskers extend 1.5 times the interquartile range from the 25th and 75th percentiles.

Lme4 package in R

Student T-Test (T.TEST function in Excel) was used whenever two samples could be compared. For multiple pairwise comparisons, we chose a linear mixed effects model. Observations were fitted to a linear mixed effects model (lmer) using lme4 package. R version 4.0.5 (2021-03-31) -- "Shake and Throw" and RStudio version 1.4.1106 “Tiger Daylily” were used with Windows 10. The genotype was the fixed effect and the experiment block was the random effect. The emmeans package was used to make pairwise comparisons between genotypes for a given bin.

Standard Error bars

We used the number of gonads to calculate SEM bars for *sygl-1* mRNA data because there are multiple mRNA/cell measurements from a single gonad. In all other cases, we used the number of experiments to calculate SEM bars because there was only one measurement per gonad.

References

Andersson, R. and Sandelin, A. (2020). Determinants of enhancer and promoter activities of regulatory elements. *Nature reviews. Genetics* **21**, 71-87.

Arnett, K. L., Hass, M., McArthur, D. G., Ilagan, M. X., Aster, J. C., Kopan, R. and Blacklow, S. C. (2010). Structural and mechanistic insights into cooperative assembly of dimeric Notch transcription complexes. *Nature structural & molecular biology* **17**, 1312-1317.

Arribere, J. A., Bell, R. T., Fu, B. X., Artiles, K. L., Hartman, P. S. and Fire, A. Z. (2014). Efficient marker-free recovery of custom genetic modifications with CRISPR/Cas9 in Caenorhabditis elegans. *Genetics* **198**, 837-846.

Austin, J. and Kimble, J. (1987). glp-1 Is required in the germ line for regulation of the decision between mitosis and meiosis in C. elegans. *Cell* **51**, 589-599.

Bailey, A. M. and Posakony, J. W. (1995). Suppressor of Hairless directly activates transcription of Enhancer of split Complex genes in response to Notch receptor activity. *Genes & development* **9**, 2609-2622.

Bentovim, L., Harden, T. T. and DePace, A. H. (2017). Transcriptional precision and accuracy in development: from measurements to models and mechanisms. *Development* **144**, 3855-3866.

Beumer, J. and Clevers, H. (2021). Cell fate specification and differentiation in the adult mammalian intestine. *Nature reviews. Molecular cell biology* **22**, 39-53.

Braude, J. P., Vijayakumar, S., Baumgarner, K., Laurine, R., Jones, T. A., Jones, S. M. and Pyott, S. J. (2015). Deletion of Shank1 has minimal effects on the molecular composition and function of glutamatergic afferent postsynapses in the mouse inner ear. *Hear Res* **321**, 52-64.

Brenner, J. L. and Schedl, T. (2016). Germline Stem Cell Differentiation Entails Regional Control of Cell Fate Regulator GLD-1 in Caenorhabditis elegans. *Genetics* **202**, 1085-1103.

Carey, M. (1991). Mechanistic advances in eukaryotic gene activation. *Current opinion in cell biology* **3**, 452-460.

Castel, D., Mourikis, P., Bartels, S. J., Brinkman, A. B., Tajbakhsh, S. and Stunnenberg, H. G. (2013). Dynamic binding of RBPJ is determined by Notch signaling status. *Genes & development* **27**, 1059-1071.

Cave, J. W., Loh, F., Surpris, J. W., Xia, L. and Caudy, M. A. (2005). A DNA transcription code for cell-specific gene activation by notch signaling. *Current biology : CB* **15**, 94-104.

Chacon-Martinez, C. A., Koester, J. and Wickstrom, S. A. (2018). Signaling in the stem cell niche: regulating cell fate, function and plasticity. *Development* **145**.

Chen, J., Mohammad, A., Pazdernik, N., Huang, H., Bowman, B., Tycksen, E. and Schedl, T. (2020). GLP-1 Notch-LAG-1 CSL control of the germline stem cell fate is mediated by transcriptional targets lst-1 and sygl-1. *PLoS Genet* **16**, e1008650.

Choi, V. N., Park, S. K. and Hwang, B. J. (2013). Clustered LAG-1 binding sites in lag-1/CSL are involved in regulating lag-1 expression during lin-12/Notch-dependent cell-fate specification. *BMB reports* **46**, 219-224.

Christensen, S., Kodoyianni, V., Bosenberg, M., Friedman, L. and Kimble, J. (1996). *lag-1*, a gene required for *lin-12* and *glp-1* signaling in *Caenorhabditis elegans*, is homologous to human CBF1 and *Drosophila* Su(H). *Development* **122**, 1373-1383.

Cinquin, O., Crittenden, S. L., Morgan, D. E. and Kimble, J. (2010). Progression from a stem cell-like state to early differentiation in the C. elegans germ line. *Proceedings of the National Academy of Sciences of the United States of America* **107**, 2048-2053.

Crittenden, S. L., Lee, C., Mohanty, I., Battula, S., Knobel, K. and Kimble, J. (2019). Sexual dimorphism of niche architecture and regulation of the Caenorhabditis elegans germline stem cell pool. *Molecular Biology of the Cell* **30**, 1757-1769.

Crittenden, S. L., Seidel, H. S. and Kimble, J. (2017). Analysis of the C. elegans Germline Stem Cell Pool. In *Germline Stem Cells* (ed. M. Buszczak), pp. 1-33. New York, NY: Springer New York.

Crocker, J., Noon, E. P. and Stern, D. L. (2016). The Soft Touch: Low-Affinity Transcription Factor Binding Sites in Development and Evolution. *Curr Top Dev Biol* **117**, 455-469.

Edelstein, A., Amodaj, N., Hoover, K., Vale, R. and Stuurman, N. (2010). Computer control of microscopes using microManager. *Curr Protoc Mol Biol* **Chapter 14**, Unit14 20.

El Mouridi, S., Lecroisey, C., Tardy, P., Mercier, M., Leclercq-Blondel, A., Zariohi, N. and Boulin, T. (2017). Reliable CRISPR/Cas9 genome engineering in Caenorhabditis elegans using a single efficient sgRNA and an easily recognizable phenotype. *G3: Genes, Genomes, Genetics* **7**, 1429-1437.

Ezer, D., Zabet, N. R. and Adryan, B. (2014). Homotypic clusters of transcription factor binding sites: A model system for understanding the physical mechanics of gene expression. *Comput Struct Biotechnol J* **10**, 63-69.

Falo-Sanjuan, J. and Bray, S. J. (2020). Decoding the Notch signal. *Dev Growth Differ* **62**, 4-14.

Falo-Sanjuan, J., Lammers, N. C., Garcia, H. G. and Bray, S. J. (2019). Enhancer Priming Enables Fast and Sustained Transcriptional Responses to Notch Signaling. *Dev Cell* **50**, 411-425 e418.

Finney, M. and Ruvkun, G. (1990). The unc-86 gene product couples cell lineage and cell identity in C. elegans. *Cell* **63**, 895-905.

Giaimo, B. D., Gagliani, E. K., Kovall, R. A. and Borggrefe, T. (2021). Transcription Factor RBPJ as a Molecular Switch in Regulating the Notch Response. *Adv Exp Med Biol* **1287**, 9-30.

Giorgetti, L., Siggers, T., Tiana, G., Caprara, G., Notarbartolo, S., Corona, T., Pasparakis, M., Milani, P., Bulyk, M. L. and Natoli, G. (2010). Noncooperative interactions between transcription factors and clustered DNA binding sites enable graded transcriptional responses to environmental inputs. *Molecular cell* **37**, 418-428.

Gomez-Lamarca, M. J., Falo-Sanjuan, J., Stojnic, R., Abdul Rehman, S., Muresan, L., Jones, M. L., Pillidge, Z., Cerda-Moya, G., Yuan, Z., Baloul, S., et al. (2018). Activation of the Notch Signaling Pathway In Vivo Elicits Changes in CSL Nuclear Dynamics. *Dev Cell* **44**, 611-623 e617.

Gopal, S., Boag, P. and Pocock, R. (2017). Automated three-dimensional reconstruction of the Caenorhabditis elegans germline. *Developmental biology* **432**, 222-228.

Gotea, V., Visel, A., Westlund, J. M., Nobrega, M. A., Pennacchio, L. A. and Ovcharenko, I. (2010). Homotypic clusters of transcription factor binding sites are a key component of human promoters and enhancers. *Genome research* **20**, 565-577.

Greenwald, I. and Kovall, R. (2013). Notch signaling: genetics and structure. *WormBook : the online review of C. elegans biology*, 1-28.

Hadwiger, G., Dour, S., Arur, S., Fox, P. and Nonet, M. L. (2010). A monoclonal antibody toolkit for C. elegans. *PloS one* **5**, e10161.

Hansen, D., Wilson-Berry, L., Dang, T. and Schedl, T. (2004). Control of the proliferation versus meiotic development decision in the C. elegans germline through regulation of GLD-1 protein accumulation. *Development* **131**, 93-104.

Hardison, R. C. and Taylor, J. (2012). Genomic approaches towards finding cis-regulatory modules in animals. *Nature reviews. Genetics* **13**, 469-483.

Haupt, K. A., Enright, A. L., Ferdous, A. S., Kershner, A. M., Shin, H., Wickens, M. and Kimble, J. (2019). The molecular basis of LST-1 self-renewal activity and its control of stem cell pool size. *Development* **146**.

Housden, B. E., Fu, A. Q., Krejci, A., Bernard, F., Fischer, B., Tavare, S., Russell, S. and Bray, S. J. (2013). Transcriptional dynamics elicited by a short pulse of notch activation involves feed-forward regulation by E(spl)/Hes genes. *PLoS Genet* **9**, e1003162.

Hubbard, E. J. A. and Schedl, T. (2019). Biology of the Caenorhabditis elegans Germline Stem Cell System. *Genetics* **213**, 1145-1188.

Jones, A. R., Francis, R. and Schedl, T. (1996). GLD-1, a Cytoplasmic Protein Essential for Oocyte Differentiation, Shows Stage- and Sex-Specific Expression duringCaenorhabditis elegansGermline Development. *Developmental biology* **180**, 165-183.

Kershner, A. M., Shin, H., Hansen, T. J. and Kimble, J. (2014). Discovery of two GLP-1/Notch target genes that account for the role of GLP-1/Notch signaling in stem cell maintenance. *Proceedings of the National Academy of Sciences of the United States of America* **111**, 3739-3744.

Kobia, F. M., Preusse, K., Dai, Q., Weaver, N., Hass, M. R., Chaturvedi, P., Stein, S. J., Pear, W. S., Yuan, Z., Kovall, R. A., et al. (2020). Notch dimerization and gene dosage are important for normal heart development, intestinal stem cell maintenance, and splenic marginal zone B-cell homeostasis during mite infestation. *PLoS Biol* **18**, e3000850.

Kuang, Y., Pyo, A., Eafergan, N., Cain, B., Gutzwiller, L. M., Axelrod, O., Gagliani, E. K., Weirauch, M. T., Kopan, R., Kovall, R. A., et al. (2021). Enhancers with cooperative Notch binding sites are more resistant to regulation by the Hairless co-repressor. *PLoS Genet* **17**, e1009039.

Lammers, N. C., Kim, Y. J., Zhao, J. and Garcia, H. G. (2020). A matter of time: Using dynamics and theory to uncover mechanisms of transcriptional bursting. *Current opinion in cell biology* **67**, 147-157.

Lee, C., Seidel, H., Lynch, T., Sorensen, E., Crittenden, S. and Kimble, J. (2017). Single-molecule RNA Fluorescence in situ Hybridization (smFISH) in Caenorhabditis elegans. *Bio-Protocol* **7**.

Lee, C., Shin, H. and Kimble, J. (2019). Dynamics of Notch-Dependent Transcriptional Bursting in Its Native Context. *Dev Cell* **50**, 426-435 e424.

Lee, C., Sorensen, E. B., Lynch, T. R. and Kimble, J. (2016). C. elegans GLP-1/Notch activates transcription in a probability gradient across the germline stem cell pool. *eLife* **5**, e18370.

Li, L., Waymack, R., Elabd, M. and Wunderlich, Z. (2021).

Lin, K. Y., Wang, W. D., Lin, C. H., Rastegari, E., Su, Y. H., Chang, Y. T., Liao, Y. F., Chang, Y. C., Pi, H., Yu, B. Y., et al. (2020). Piwi reduction in the aged niche eliminates germline stem cells via Toll-GSK3 signaling. *Nat Commun* **11**, 3147.

Madani Tonekaboni, S. A., Mazrooei, P., Kofia, V., Haibe-Kains, B. and Lupien, M. (2019). Identifying clusters of cis-regulatory elements underpinning TAD structures and lineage-specific regulatory networks. *Genome research* **29**, 1733-1743.

Melton, C., Reuter, J. A., Spacek, D. V. and Snyder, M. (2015). Recurrent somatic mutations in regulatory regions of human cancer genomes. *Nature genetics* **47**, 710-716.

Muncie, J. M. and Weaver, V. M. (2018). The Physical and Biochemical Properties of the Extracellular Matrix Regulate Cell Fate. *Curr Top Dev Biol* **130**, 1-37.

Nam, Y., Sliz, P., Pear, W. S., Aster, J. C. and Blacklow, S. C. (2007). Cooperative assembly of higher-order Notch complexes functions as a switch to induce transcription. *Proceedings of the National Academy of Sciences of the United States of America* **104**, 2103-2108.

Nellesen, D. T., Lai, E. C. and Posakony, J. W. (1999). Discrete Enhancer Elements Mediate Selective Responsiveness of Enhancer of split Complex Genes to Common Transcriptional Activators. *Developmental biology*, 33-53.

Neves, A., English, K. and Priess, J. R. (2007). Notch-GATA synergy promotes endoderm-specific expression of ref-1 in C. elegans. *Development* **134**, 4459-4468.

Paix, A., Folkmann, A., Rasoloson, D. and Seydoux, G. (2015). High Efficiency, Homology-Directed Genome Editing in Caenorhabditis elegans Using CRISPR-Cas9 Ribonucleoprotein Complexes. *Genetics* **201**, 47-54.

Park, J., Estrada, J., Johnson, G., Vincent, B. J., Ricci-Tam, C., Bragdon, M. D., Shulgina, Y., Cha, A., Wunderlich, Z., Gunawardena, J., et al. (2019). Dissecting the sharp response of a canonical developmental enhancer reveals multiple sources of cooperativity. *Elife* **8**.

Payne, J. L. and Wagner, A. (2015). Mechanisms of mutational robustness in transcriptional regulation. *Front Genet* **6**, 322.

Perez-Gonzalez, C., Ceada, G., Greco, F., Matejcic, M., Gomez-Gonzalez, M., Castro, N., Menendez, A., Kale, S., Krndija, D., Clark, A. G., et al. (2021). Mechanical compartmentalization of the intestinal organoid enables crypt folding and collective cell migration. *Nature cell biology* **23**, 745-757.

Ptashne, M. (1988). How eukaryotic transcriptional activators work. *Nature* **335**, 683-689.

Richardson, C. D., Ray, G. J., DeWitt, M. A., Curie, G. L. and Corn, J. E. (2016). Enhancing homology-directed genome editing by catalytically active and inactive CRISPR-Cas9 using asymmetric donor DNA. *Nat Biotechnol* **34**, 339-344.

Sadeghi, S. G., Pyott, S. J., Yu, Z. and Glowatzki, E. (2014). Glutamatergic signaling at the vestibular hair cell calyx synapse. *J Neurosci* **34**, 14536-14550.

Schindelin, J., Arganda-Carreras, I., Frise, E., Kaynig, V., Longair, M., Pietzsch, T., Preibisch, S., Rueden, C., Saalfeld, S. and Schmid, B. (2012). Fiji: an open-source platform for biological-image analysis. *Nature methods* **9**, 676-682.

Severson, E., Arnett, K. L., Wang, H., Zang, C., Taing, L., Liu, H., Pear, W. S., Shirley Liu, X., Blacklow, S. C. and Aster, J. C. (2017). Genome-wide identification and characterization of Notch transcription complex–binding sequence-paired sites in leukemia cells. *Science Signaling* **10**, eaag1598.

Shin, H., Haupt, K. A., Kershner, A. M., Kroll-Conner, P., Wickens, M. and Kimble, J. (2017). SYGL-1 and LST-1 link niche signaling to PUF RNA repression for stem cell maintenance in Caenorhabditis elegans. *PLoS Genet* **13**, e1007121.

Shlyueva, D., Stampfel, G. and Stark, A. (2014). Transcriptional enhancers: from properties to genome-wide predictions. *Nature reviews. Genetics* **15**, 272-286.

Siegfried, K. R. and Kimble, J. (2002). POP-1 controls axis formation during early gonadogenesis in C. elegans.

Spitzer, M., Wildenhain, J., Rappsilber, J. and Tyers, M. (2014). BoxPlotR: a web tool for generation of box plots. *Nature methods* **11**, 121-122.

Starich, T. and Greenstein, D. (2020). A Limited and Diverse Set of Suppressor Mutations Restore Function to INX-8 Mutant Hemichannels in the Caenorhabditis elegans Somatic Gonad. *Biomolecules* **10**.

Stern, D. L. and Orgogozo, V. (2009). Is genetic evolution predictable? *Science* **323**, 746-751.

Torella, R., Li, J., Kinrade, E., Cerda-Moya, G., Contreras, A. N., Foy, R., Stojnic, R., Glen, R. C., Kovall, R. A., Adryan, B., et al. (2014). A combination of computational and experimental approaches identifies DNA sequence constraints associated with target site binding specificity of the transcription factor CSL. *Nucleic Acids Res* **42**, 10550-10563.

Tun, T., Hamaguchi, Y., Matsunami, N., Furukwawa, T., Honjo, T. and Kawaichi, M. (1994). Recognition sequence of a highly conserved DNA binding protein RBP-Jx. *Nucleic Acids Research* **22**, 965-971.

Wang, H., Zang, C., Taing, L., Arnett, K. L., Wong, Y. J., Pear, W. S., Blacklow, S. C., Liu, X. S. and Aster, J. C. (2014). NOTCH1-RBPJ complexes drive target gene expression through dynamic interactions with superenhancers. *Proceedings of the National Academy of Sciences of the United States of America* **111**, 705-710.

Wong, F. and Gunawardena, J. (2020). Gene Regulation in and out of Equilibrium. *Annual review of biophysics* **49**, 199-226.

Yoo, A. S., Bais, C. and Greenwald, I. (2004). Crosstalk Between the EGFR and LIN-12/Notch Pathways in C. elegans Vulval Development. *Science* **303**, 663-667.

Figure 1
Lynch et al.

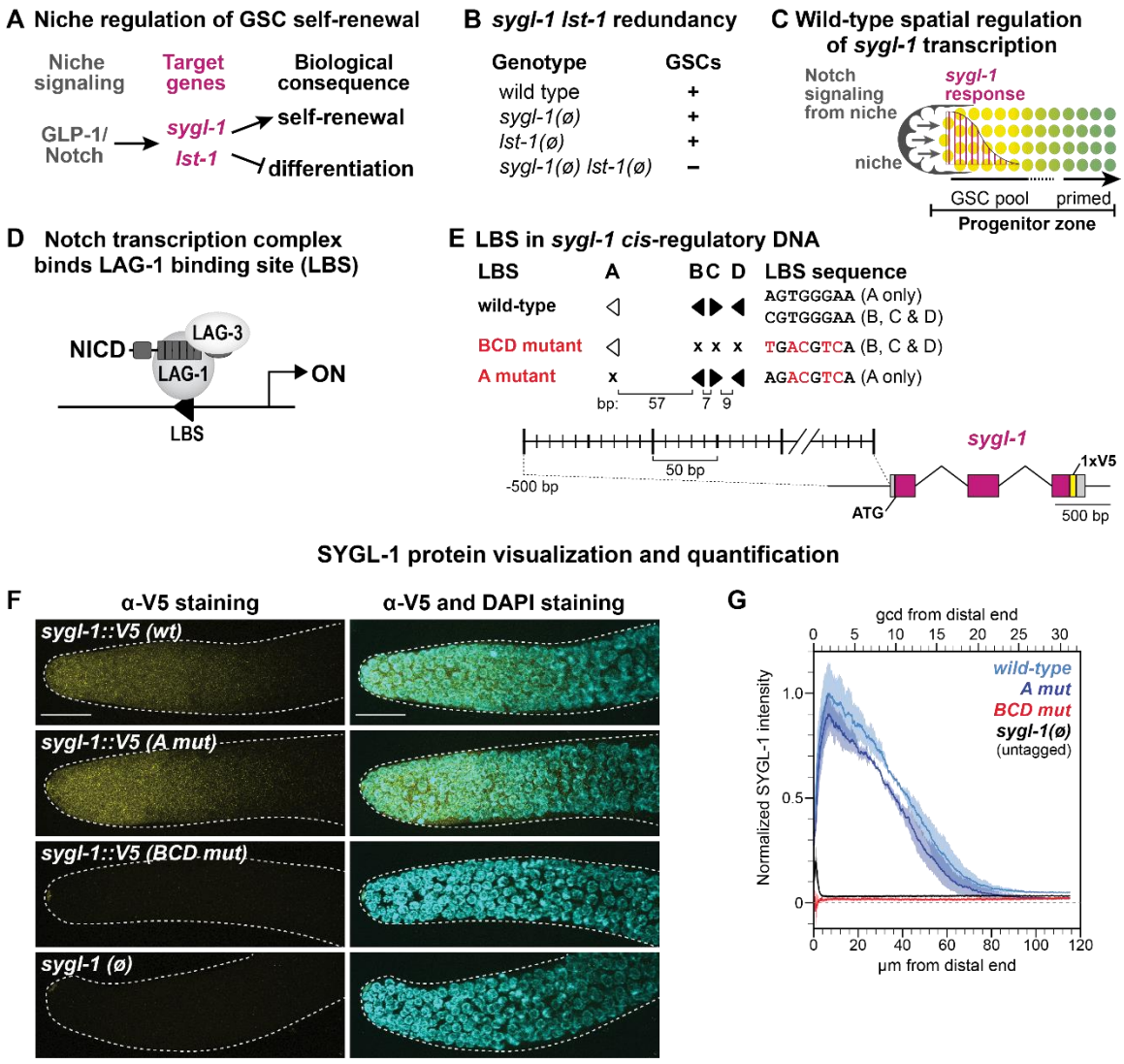

Figure 1. Identification of functional LBSs in *sygl-1 cis*-regulatory DNA.
A. *C. elegans* germline stem cell (GSC) molecular regulators. **B.** Loss of either *sygl-1* or *lst-1* permits adult GSC self-renewal, but loss of both produces a Glp phenotype (small sterile germline, loss of GSCs). **C.** *C. elegans* distal gonad. The niche (gray) is a somatic cell at the distal end. GLP-1/Notch signaling (arrows) maintains a pool of GSCs in the distal progenitor zone (yellow) and activates graded *sygl-1* transcription (magenta). Germ cells in the proximal progenitor zone become primed for differentiation (green). **D.** Trimeric Notch transcriptional activation complex: Notch intracellular domain (NICD), Mastermind-like coactivator (LAG-3 in *C. elegans*), CSL DNA-binding member (LAG-1 in *C. elegans*). **E.** Filled arrowheads: canonical 5' YGTGRGAA 3' LBS; open arrowheads: noncanonical. Arrowheads point right for 5' CGTGGGAA 3' and left for its complement 5' TTCCCACG 3'. Mutant LBS (x): 5' TGACGTCA 3' for LBS B, C, and D ; 5' AGACGTCA 3' for LBS A. Spacing in bp between each LBS is shown to scale. A 1xV5 epitope tag (yellow) was inserted just before the stop codon to visualize SYGL-1 protein. Exons, magenta; UTRs, gray. **F.** Representative maximum-intensity z-projections of V5-stained dissected distal gonads. Scale bar: 20 µm. Strain genotypes listed in Table S1. **G.** FIJI quantification of α-V5 signal normalized to *sygl-1::V5(wt)* (see Methods). Position measures are germ cell diameters (gcd) above and microns (µm) below. Total gonads scored from two independent experiments: *wt*, 29; *A mut*, 31; *BCD mut*, 25; *sygl-1(ø)*, 24.

Figure 2
Lynch et al.

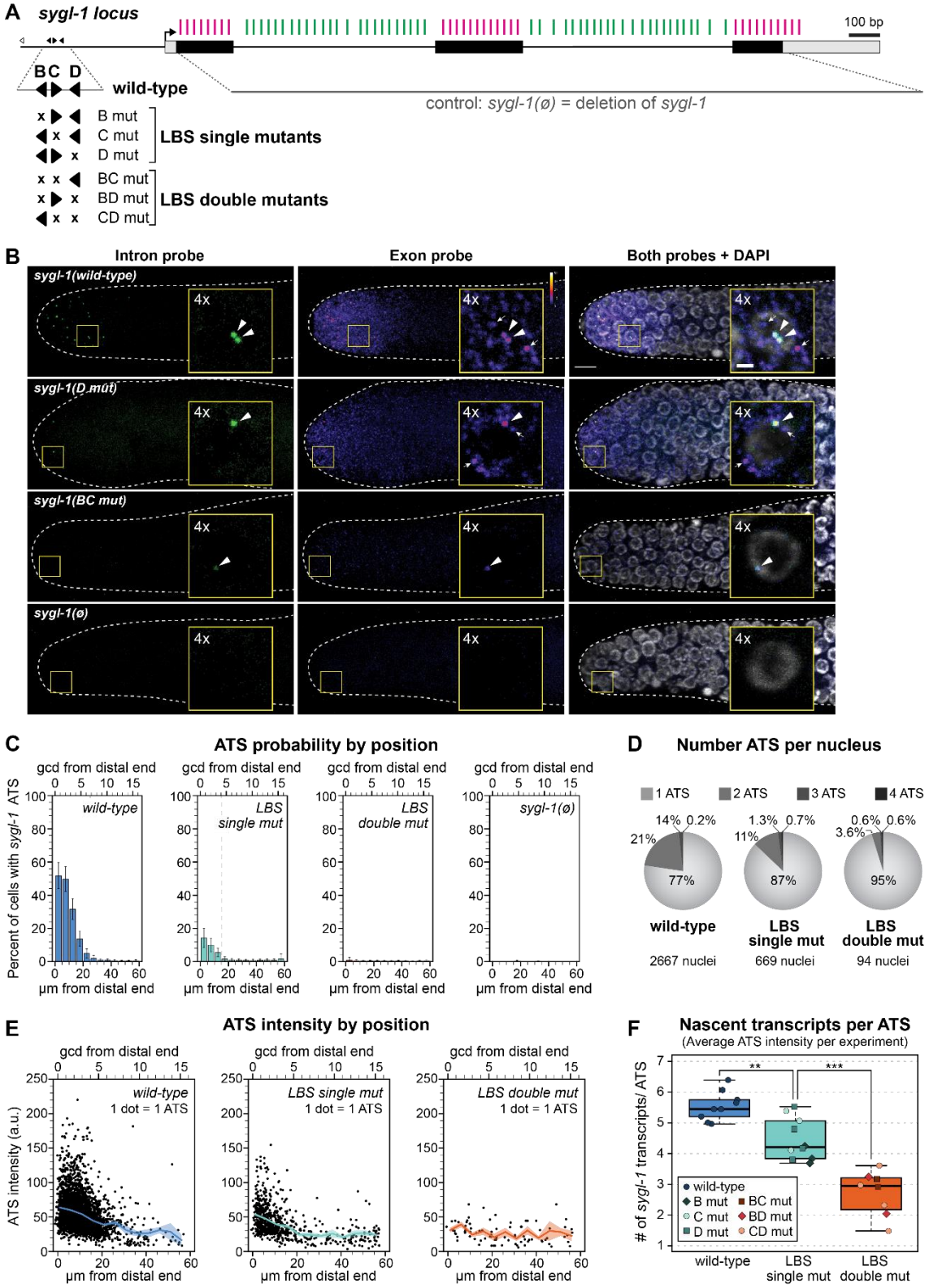

Figure 2: LBS mutations weaken niche-dependent transcriptional response of *sygl-1*

A. Black boxes: exons; gray boxes: untranslated regions; black arrow: predicted transcription start site; smFISH probes to exons (magenta) and introns (green) (see Methods). The *sygl-1(ø)* control removes *sygl-1* sequence that probes detect. Expansion shows individual LBSs and their mutations; conventions as in Fig1E. LBS mutants in this figure are not V5-tagged. **B.** Representative images of *sygl-1* smFISH in distal end of dissected gonads. Exon channel colors reflect intensity to show mRNA without saturating ATS (see Methods; color key in upper right; pixel intensities 3-50). DAPI shown in grayscale. Main images: maximum-intensity z-projections; insets: 4x-magnified maximum-intensity projections (four 0.3 µm slices). Arrowheads: ATS (overlapping intron/exon/DAPI). Arrows: cytoplasmic mRNA (exon only). Strain genotypes listed in Table S1. **C-F.** See Fig S2E for details (e.g. total # gonads scored. **C.** Percentage of nuclei with ≥1 ATS as a function of distance (units as in Fig 1G). Extent of transcription indicated by gray dashed line (where <5% cells contain ≥1 ATS). Error bars: SEM. **D.** Numbers in pie charts are averages between experiments (see Methods). Nuclei with zero *sygl-1* ATS excluded. **E.** Each dot represents one ATS (see Methods); see Fig S2D for details (e.g. total ATS scored). Solid line: mean (5 µm intervals); shaded: SEM. **F.** ATS intensities ÷ 10 roughly estimate # primary transcripts/ATS (see Methods). Boxplot center lines: median (wt: 5.1; singles; 3.7; doubles: 2.6); see Methods for BoxPlotR conventions. Each dot represents mean of all ATS/experiment (irrespective of position). Total # experiments: wt: 9; singles: 10; doubles: 8. Experiments with zero ATS detected (*BC mut*, *BD mut*) are not represented.

Figure 3
Lynch et al.

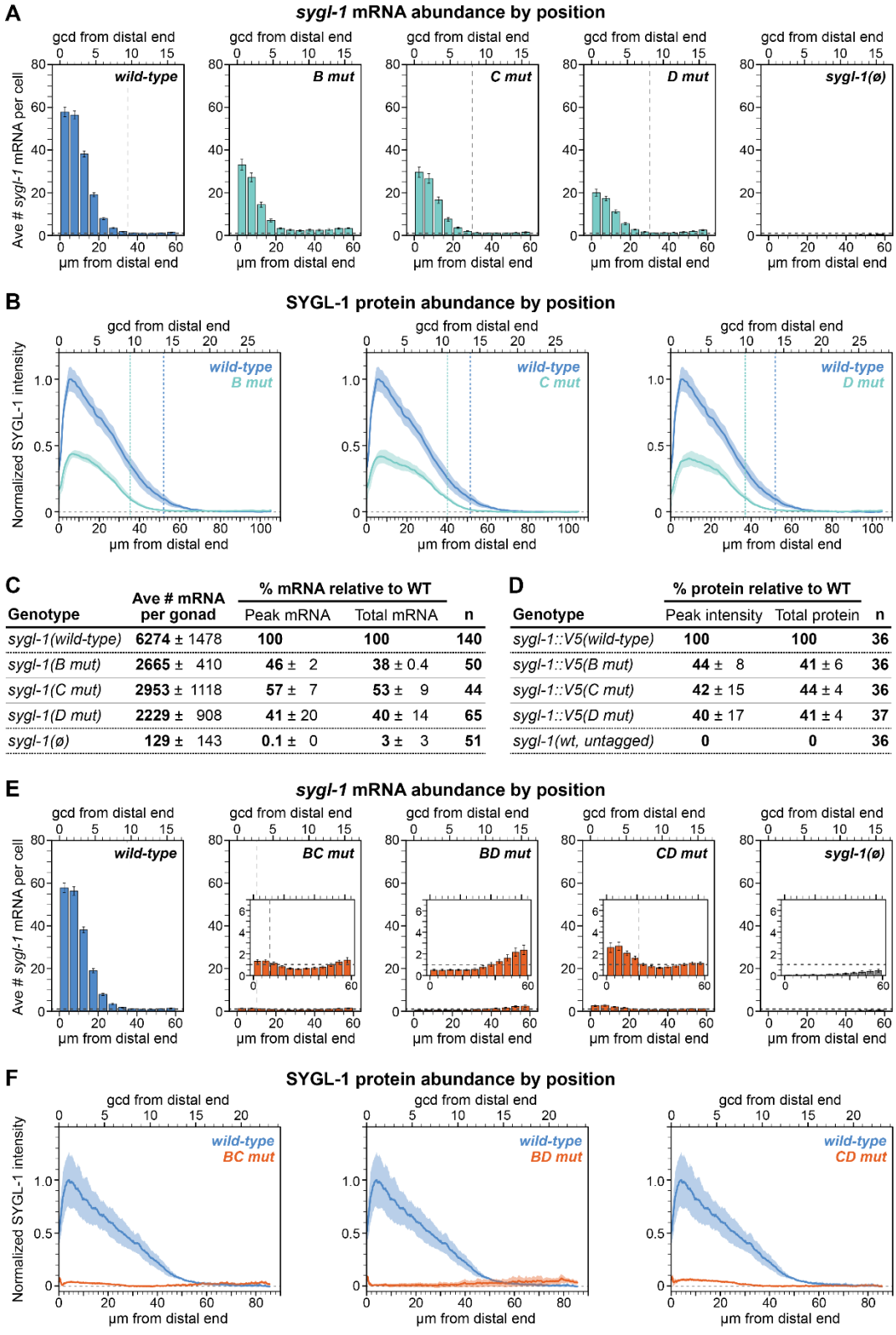

C

Genotype	Ave # mRNA per gonad	% mRNA relative to WT: Peak mRNA	% mRNA relative to WT: Total mRNA	n
sygl-1(wild-type)	**6274** ± 1478	**100**	**100**	**140**
sygl-1(B mut)	**2665** ± 410	**46** ± 2	**38** ± 0.4	**50**
sygl-1(C mut)	**2953** ± 1118	**57** ± 7	**53** ± 9	**44**
sygl-1(D mut)	**2229** ± 908	**41** ± 20	**40** ± 14	**65**
sygl-1(ø)	**129** ± 143	**0.1** ± 0	**3** ± 3	**51**

D

Genotype	% protein relative to WT: Peak intensity	% protein relative to WT: Total protein	n
sygl-1::V5(wild-type)	**100**	**100**	**36**
sygl-1::V5(B mut)	**44** ± 8	**41** ± 6	**36**
sygl-1::V5(C mut)	**42** ± 15	**44** ± 4	**36**
sygl-1::V5(D mut)	**40** ± 17	**41** ± 4	**37**
sygl-1(wt, untagged)	**0**	**0**	**36**

Figure 3: Molecular *sygl-1* output is reduced

RNA data from smFISH experiments (Fig. A, C, E) and protein data from α-V5 staining (Fig. B, D, F) were both measured in an *lst-1(+)* background. Strain genotypes listed in Table S1; all data is from adult animals. **A-D.** LBS single mut *sygl-1* mRNA and protein are reduced to approximately half of wild-type. **E-F.** LBS double mut *sygl-1* mRNA and protein are reduced to near zero. In Fig. 3E, insets are used to better visualize where mRNA is above or below background. **A,E.** Average # *sygl-1* mRNA/cell (see Methods). Position measures as in Fig 1G. Error bars: SEM. Vertical dashed lines: spatial extent, where values fall below background and/or reach minimum. Horizontal dashed lines: background (from *sygl-1(ø)*, see Methods). Total # gonads scored: see Fig S2E. **B,F.** Quantification of α-V5 immunofluorescence (see Methods). Solid lines: mean; shading: SEM. y axis "0" (dashed line) represents values from untagged control. Small peaks 0-3 µm from distal end are nonspecific V5 signal (see Methods). Dashed lines: spatial extent, where values fall below 10% WT maximum. Total # gonads scored in Fig. 3B listed in Fig3D; total gonads scored in Fig 3F from 3-4 experiments: *wt*: 61; *BC mut*: 49; *BD mut*: 59 *CD mut*: 39. **C.** Summary of mRNA data in LBS single mutants. Numbers are mean per experiment ± standard deviation between experiments (see Methods). n: # gonads scored in ≥3 experiments. Peak: mRNA/cell values from the 0-5 µm region as a percent of wild-type; total: numbers of mRNA per gonad as a percent of wild-type. **D.** Summary of protein data in LBS single mutants. Numbers are mean percentage of wild-type for each replicate ± standard deviation between replicates (see Methods). n: total gonads scored in 3 replicates.

A **Germline function in *lst-1(ø) sygl-1(x)* mutants**

genotype *lst-1*	genotype *sygl-1*	*sygl-1 LBS* B	C	D	% fertile*	n[1]	% Glp†	n[2]
ø	*wild-type*	◀	▶	◀	99	133	0	141
ø	*B mut*	x	▶	◀	98	107	0	106
ø	*C mut*	◀	x	◀	96	118	0	73
ø	*D mut*	◀	▶	x	98	114	0	97
ø	*BC mut*	x	x	◀	0	> 100	100	24
ø	*BD mut*	x	▶	x	0	> 100	100	19
ø	*CD mut*	◀	x	x	0	> 100	100	19

* : % of homozygous young adults with embryo-containing uteri
† : % Glp gonads (small, loss of GSCs, sperm at distal end)
n[1]: number of animals scored for fertility
n[2]: number of gonads scored for Glp phenotype

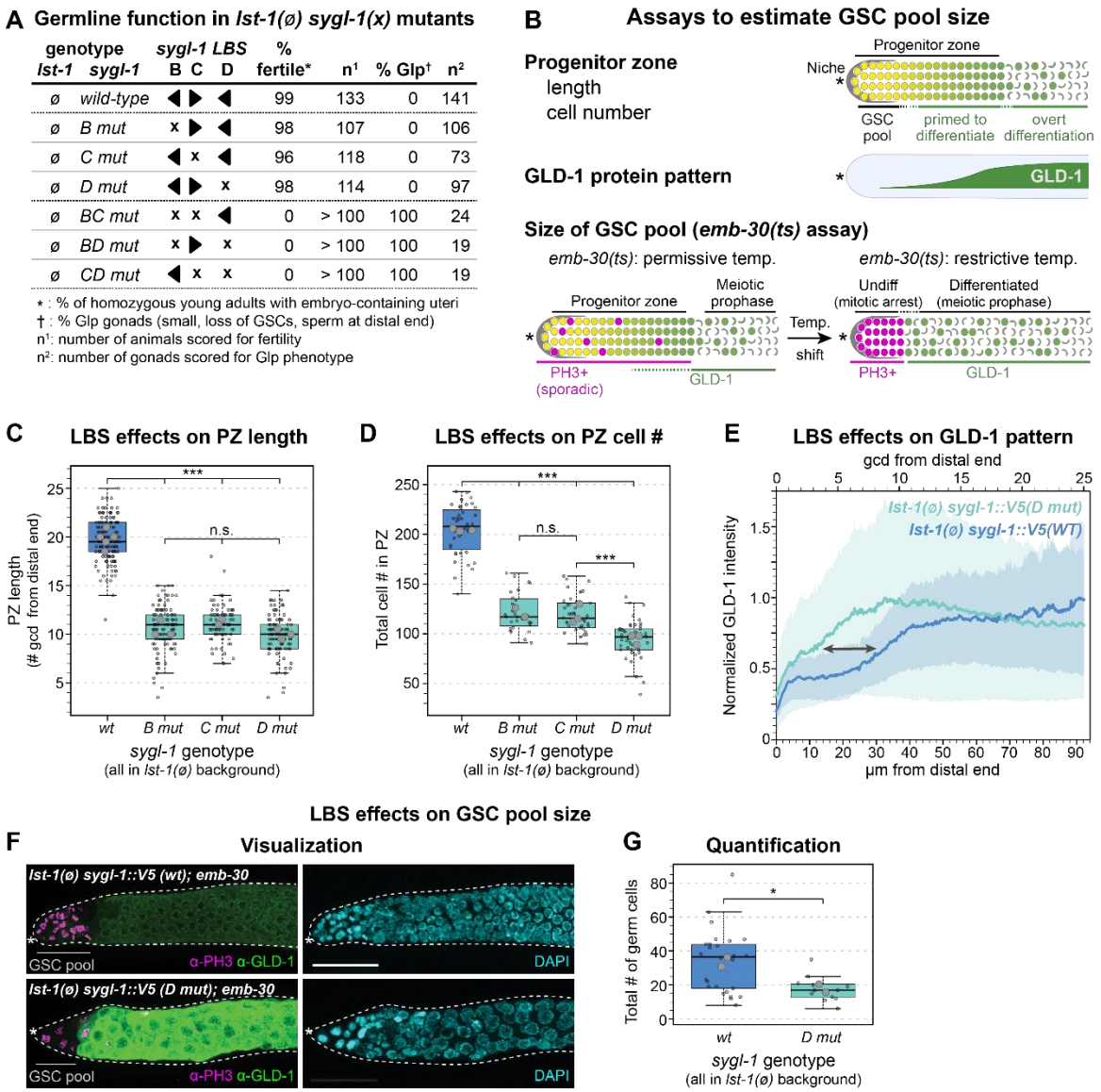

Figure 4: Effect of SYGL-1 abundance on GSC pool size

A. Percent of fertile animals was scored at low magnification and percent Glp animals scored at high magnification. The same gonads scored for %Glp (Fig4A) were used to score PZ length (Fig4C). **B.** Top, Progenitor Zone (PZ) includes distal GSC pool and GSC daughters primed to differentiate. Overt differentiation: visible meiotic prophase. Middle, increased GLD-1 protein reflects differentiation. Bottom, GSC pool size estimation; temperature-sensitive (ts). Left: at 15°C, *lst-1(ø) sygl-1(x); emb-30(ts)* PZ contains scattered M-phase (PH3+, magenta) cells and gradual increase in GLD-1 (green). Right: when shifted to 25°C, PZ germ cells arrest, defining two populations, mitotically-arrested distal PH3+ cells (inferred to be GSCs) and proximal GLD-1+, PH3-negative cells (inferred to be GSC daughters). *: distal end. **A, C-G.** Strain genotypes in Table S1. **C-D.** Boxplot conventions match Fig 2F. Small translucent data points: individual gonads; larger data points: replicate averages. Data collected from each gonad were fitted to a linear mixed effects model; Tukey's post-hoc test was used to make pairwise comparisons between genotypes. ***: $p < 0.0001$; n.s., not significant ($p \geq 0.01$). **C.** Average # germ cell diameters (gcd) in PZ were counted by eye. Total gonads scored in 2-5 experiments: *wt*: 141; *B mut*: 106; *C mut*: 73; *D mut*: 97. **D.** Total # cells in PZ were counted with Imaris software (see Methods). Total gonads scored in 3 independent experiments: *wt*: 40; *B mut*: 28; *C mut*: 42; *D mut*: 42. **E.** Fixed adult gonads were stained with

polyclonal antibody to GLD-1 (gift from T. Schedl). Gray arrow: distal shift of GLD-1 accumulation. Position measures as in Fig. 1G. Signal intensities normalized against internal controls (see Methods). Solid lines: mean; shading: SEM. 24 gonads/genotype scored from 2 replicates. **F.** Representative maximum-intensity projections. Left, α-PH3 (magenta), α-GLD-1 (green). Gray line: relative lengths of GSC pools. Right, DAPI (cyan); scale bar: 20 µm. **G.** Estimated # GSCs in naïve pool; GLD-1-negative PH3+ cells were manually counted in FIJI. Boxplot conventions are as in Fig 2F, 5C-D. Total gonads scored in 2 experiments: *wt*: 26; *D mut*: 12. Meiotic gonads excluded from *D mut* (see Methods). *: p = 0.05. Student's two-tailed T-test conducted on replicate averages; homoscedasticity assumed.

Figure 5
Lynch et al.

A **LBS effects on PZ length**

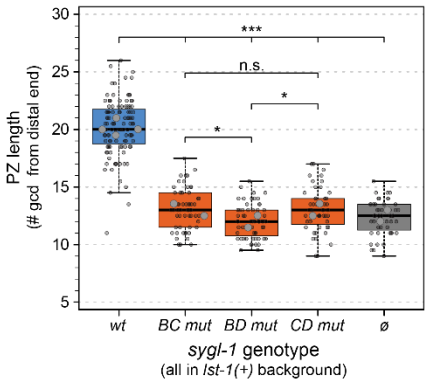

B **LBS effects on germ cell state and number**

sygl-1 genotype*	% undiff.	% diff.	# germ cells	n
sygl-1(ø)/+	100	0	**>100**	42
sygl-1(BC mut)	0	100	**44** ± 1.8	39
sygl-1(BD mut)	0	100	**8** ± 0.7	36
sygl-1(CD mut)	0	100	**43** ± 0.6	28
sygl-1(ø)	0	100	**7** ± 0.8	34

*all in *lst-1(ø)* background

C

Example:
BC mut
Ave # mRNA/cell
in first 5 µm = 1.4

mRNA distributed evenly
could be explained by false positives

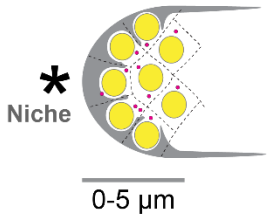

11 mRNA in 8 of 8 cells = 1.4 mRNA/cell
mRNA/cell ~= average (1-2)

mRNA concentrated in a few cells
consistent with stochastic txl bursts

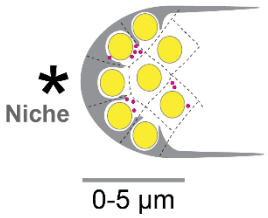

11 mRNA in 3 of 8 cells = 1.4 mRNA/cell
mRNA/cell > average (3 or 5)

D **LBS effects on mRNA number, scored in individual cells containing "x" # *sygl-1* mRNA**

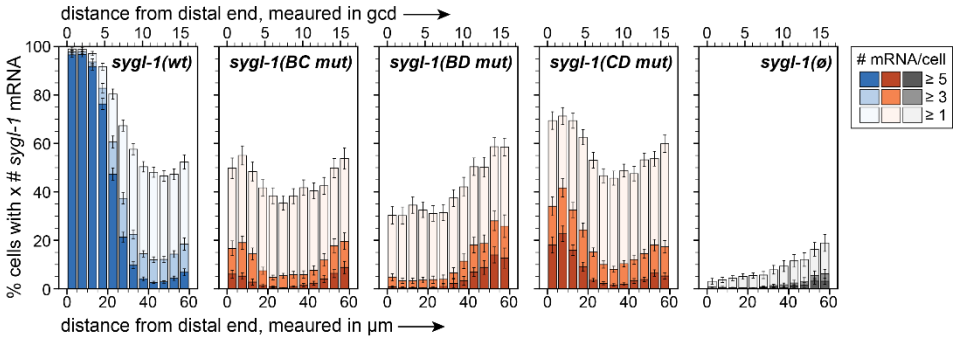

Figure 5: LBS double mutants probe individual LBS equivalence

A-C. Strain genotypes in Table S1. **A.** Boxplot conventions match Fig 4C-D. Total gonads scored in 2-4 experiments: *wt*: 111; *BC mut*: 57; *BD mut*: 59; *CD mut*: 48; *sygl-1(ø)*: 48. Linear mixed effects model and Tukey's post-hoc used as in Fig4C-D. *: $p < 0.05$ ($p = 0.04$ in both cases); *** $p < 0.0001$. All other pairwise comparisons are not significant (n.s.: $p > 0.05$). Not all n.s. comparisons shown. **B.** Total # germ cells (both gonad arms); average/replicate ± standard deviation between replicates. Percent of animals were scored as undifferentiated (undiff) or differentiated (diff) by their distalmost germ cells using DAPI morphology and/or SP56+ staining, and germ cell numbers were extrapolated (see Methods). n: total gonads scored in 2-4 experiments. Control was JK6401. **C.** Two explanations of an average of 1.4 mRNA/cell in a troop of ~8 cells (see Fig S4A). Left: 1-2 mRNAs in all cells; Right: no RNAs in some cells and 3-5 mRNAs in others. **D.** Percentage of total nuclei that contain ≥1, ≥3, or ≥5 *sygl-1* mRNA in each bin of distance from the distal end (Methods). Position measures as in Fig 1G. Error bars: SEM. Strains in *lst-1(+)* background.

Figure 6
Lynch et al.

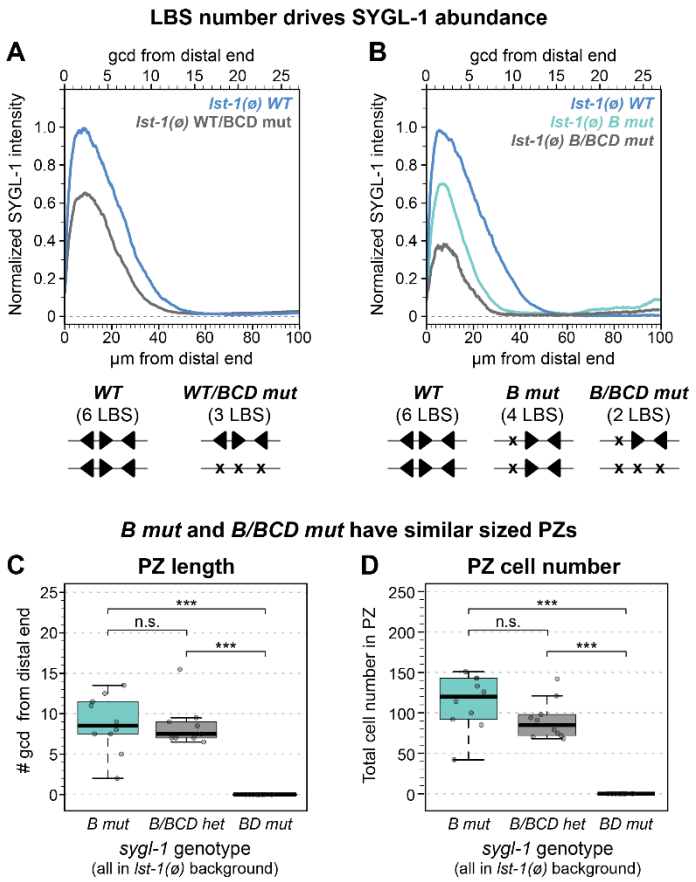

E **LBS paradox**

		% of WT SYGL-1	Inferred activity of LBS C
LBS C only (*BD mut*)		~0%	negligible
LBS C loss (*C mut*)		~50%	substantial

Figure 6. LBS number is a key factor in determining SYGL-1 abundance

A-B. Quantification of α-V5 immunofluorescence. Conventions as in Fig 3C, except only mean shown (Methods). See Methods for *sygl-1* heterozygote creation. **A.** 30 gonads per genotype scored in 2 experiments. **B.** Total gonads scored in 1-4 experiments: *wt*: 66; *B mut*: 73; *B/BCD mut*: 10; *BD mut*: 10. **C-D.** Boxplot conventions match Fig 2F. ***: P<0.01, n.s.: p≥0.01; Student's two-tailed T-test (homoscedasticity assumed). 10 gonads per genotype scored from one experiment. **C.** Average # germ cell diameters (gcd) in PZ were counted by eye. p = 0.86 (*B mut* vs *B/BCD mut*). **D.** Total # cells in PZ counted using Imaris (see Methods). p = 0.11 (*B mut* vs *B/BCD mut*). **E.** Results in LBS single and double mutants are paradoxical; see text for explanation.

Figure 7
Lynch et al.

A **Gradient shape in LBS single mutants**

Molecular metrics	1° transcripts (%wt)	mRNA (% wt)	protein (% wt)
Abundance at peak (a.u.)	27%	47%	42%
Extent along gonadal axis (µm)	60%	86%	71%
Sum (area under curve, a.u.)	19%	44%	42%

B **Spacing and polarity of intact LBS in single mutants**

sygl-1 LBS	spacing	polarity
B mut	9 nt	head-to-head
C mut	24 nt	head-to-tail
D mut	7 nt	tail-to-tail

Figure 7. Summary of functional LBS analysis

A. Descriptors of gradient shape (as a percentage of wild-type): abundance at peak (0-5 µm from the distal end, varying units); extent (distance along gonadal axis in µm); sum (area under curve, in arbitrary units). *B mut*, *C mut*, and *D mut* values were averaged together into a single LBS single mut value (See Methods). 1°: primary (nascent) transcripts. **B.** Each pair of LBSs in single mutants drives similar synergy as any other pair, despite differences in spacing and polarity. Arrowhead conventions match Fig 1E.